

Summary of the GK15 Ground-Motion Prediction Equation for Horizontal PGA and 5% Damped PSA from Shallow Crustal Continental Earthquakes

by Vladimir Graizer and Erol Kalkan

Abstract We present a revised ground-motion prediction equation (GMPE) for computing medians and standard deviations of peak ground acceleration (PGA) and 5% damped pseudospectral acceleration (PSA) response ordinates of the horizontal component of randomly oriented ground motions to be used for seismic-hazard analyses and engineering applications. This GMPE is derived from the expanded Next Generation Attenuation (NGA)-West 1 database (see [Data and Resources](#); [Chiou *et al.*, 2008](#)). The revised model includes an anelastic attenuation term as a function of quality factor (Q_0) to capture regional differences in far-source (beyond 150 km) attenuation, and a new frequency-dependent sedimentary-basin scaling term as a function of depth to the 1.5 km/s shear-wave velocity isosurface to improve ground-motion predictions at sites located on deep sedimentary basins. The new Graizer–Kalkan 2015 (GK15) model, developed to be simple, is applicable for the western United States and other similar shallow crustal continental regions in active tectonic environments for earthquakes with moment magnitudes (M) 5.0–8.0, distances 0–250 km, average shear-wave velocities in the upper 30 m (V_{S30}) 200–1300 m/s, and spectral periods (T) 0.01–5 s. Our aleatory variability model captures interevent (between-event) variability, which decreases with magnitude and increases with distance. The mixed-effect residuals analysis reveals that the GK15 has no trend with respect to the independent predictor parameters. Compared to our 2007–2009 GMPE, the PGA values are very similar, whereas spectral ordinates predicted are larger at $T < 0.2$ s and they are smaller at longer periods.

Introduction

In earthquake-prone regions, design of new or evaluation of existing structures relies on prediction of ground shaking. The level of ground shaking is frequently defined using ground-motion prediction equations (GMPEs) that are a function of earthquake magnitude, style of faulting, site-to-source distance, and site parameters. GMPEs are often, in empirical form, guided by earthquake physics and/or simulations, and their estimator coefficients are typically computed by single or multistage regression on ground-motion amplitudes recorded from previous earthquakes.

An initial GMPE for peak ground acceleration (PGA) and 5% damped pseudospectral acceleration (PSA) response ordinates of the horizontal component of randomly oriented ground motions was developed by [Graizer and Kalkan \(2007, 2009\)](#) using the Next Generation Attenuation (NGA)-West1 database (see [Data and Resources](#); [Chiou *et al.*, 2008](#)) along with additional records from major California earthquakes, including the 2004 Parkfield (M 6.0, M , moment magnitude) and 2003 San Simeon (M 6.5) earthquakes, and a

number of smaller magnitude (5.0–5.7) earthquakes from Turkey, California, and other shallow crustal continental regions.

The new Graizer–Kalkan GMPE (GK15) is composed of two predictive equations. The first equation predicts PGA ([Graizer and Kalkan, 2007](#)), and the second equation constructs the spectral shape ([Graizer and Kalkan, 2009](#)). The term spectral shape refers to the PSA response spectrum normalized by PGA. The PSA response spectrum is obtained by anchoring the spectral shape to the PGA. In this model, the PSA response spectrum is a continuous function of the spectral period (T). Typically GMPEs (e.g., NGA-West 2 models of [Abrahamson *et al.*, 2014](#); [Boore *et al.*, 2014](#); [Campbell and Bozorgnia, 2014](#); [Chio and Youngs, 2014](#)) use a discrete functional form for predicting the PSA response ordinates. The concept of a continuous function assumes cross correlation of spectral ordinates at different periods ([Baker, 2011](#)), and de facto eliminates the difference between period intervals by making period intervals infinitesimally short. As a

Table 1

List of Abbreviations and Symbols Present in This Article

B_{depth}	Basin depth under the site in kilometers
C	Constant term from the mixed-effects analysis
F	Style of faulting
G_1	Scaling function for magnitude and style of faulting
G_2	Path scaling function
G_3	Anelastic attenuation function
G_4	Site amplification function
G_5	Basin scaling function
GK15	Graizer and Kalkan (2015)
GMPE	Ground-motion prediction equation
I	Peak spectral intensity
M	Moment magnitude
PGA	Peak ground acceleration
R	Closest distance to fault rupture plane
Res_{ij}	Residual of j th recording of i th earthquake
Q_0	Regional quality factor
S	Spectral wideness (area under the spectral shape)
PSA	Pseudospectral acceleration
PSA_{norm}	Spectral shape (i.e., normalized response spectrum by PGA)
T	Spectral period
$T_{\text{sp},0}$	Predominant period of the response spectrum
V_{530}	Shear-wave velocity in the upper 30 m of the geological profile
$Z_{1.5}$	Depth to 1.5 km/s shear-wave velocity isosurface in kilometer
σ	Total standard deviation
μ	Function defining predominant period of the response spectrum
μ_i	Event term for event i
ϵ_{ij}	Intraevent residual for recording j in event i
τ	Standard deviation of event term
ϕ	Standard deviation of intraevent term
ζ	Decay function of the PSA response spectrum at long periods

consequence, a long list of estimator coefficients for a range of spectral periods is eliminated, and spectral ordinates are estimated smoothly.

Our predictive equations for PGA and spectral shape constitute a series of functions guided by empirical data and simulations. Each function represents a physical phenomenon affecting the ground-motion attenuation. We refer to these functions as filters. Although the filter concept (i.e., linear system theory) is strictly valid for Fourier spectrum, we adapted a similar approach for modeling ground-motion prediction, which has been shown to be accurate (expected median prediction without significant bias with respect to the independent predictor parameters) and efficient (relatively small epistemic variability) ([Graizer and Kalkan, 2009, 2011, 2015](#); [Graizer et al., 2013](#)).

This article presents a summary of our recent improvements on GK15, and provides a complete description of the basis for its functional form. The recent NGA-West2 project ([Bozorgnia et al., 2014](#)) and new data (e.g., [Baltay and Boatwright, 2015](#)) indicate a need to include regionalization when accounting for differences in far-source (beyond 150 km) distance attenuation of ground motions and soil response. Motivated by this need, the updates include a new anelastic attenuation term as a function of quality factor to capture regional differences in far-source attenuation, and a new fre-

quency-dependent sedimentary-basin scaling term as a function of depth to the 1.5 km/s shear-wave velocity isosurface to improve ground-motion predictions for sites on deep sedimentary basins. We believe that these changes represent major improvements to our previous GMPE ([Graizer and Kalkan, 2007, 2009](#)), and therefore justify the additional complexity in GK15. The analysis of mixed-effect residuals reveals that the revised GMPE is unbiased with respect to its independent predictor parameters.

In the following, we first describe the selection of data used in this update. We then present the changes made, followed by evaluations of the updated model and comparisons to the observations and recent NGA-West2 models. Finally, we offer some guidance on model applicability. The list of abbreviations and symbols used throughout this article is given in Table 1. Additional technical information on GK15 GMPE can be found in [Graizer and Kalkan \(2015\)](#).

Intensity Measures

The ground-motion intensity measures (IMs) comprising the dependent variables of the GMPE include horizontal-component PGA and 5% damped PSA. These IMs were computed from the randomly oriented geometric mean of the two horizontal components of ground motions. We do not include predictive equations for peak ground velocity or displacement yet.

Selection of Ground-Motion Data

A total of 2583 ground-motion recordings from 47 shallow crustal continental earthquakes with focal depths less than 20 km were selected. This dataset includes events gathered from the Pacific Earthquake Engineering Research Center database created under the NGA-West1 project (see [Data and Resources](#); [Chiou et al., 2008](#)) and data from a number of additional events and stations. Specifically, data from the following earthquakes were included: 1994 M 6.7 Northridge, 1999 M 7.1 Hector Mine, 2003 M 4.9 Big Bear City, 2003 M 6.5 San Simeon, 2004 M 6.0 Parkfield, 2005 M 5.2 Anza and M 4.9 Yucaipa, 1976 M 6.8 Gazli (Uzbekistan), 1988 M 6.8 Spitak (Armenia), 1991 M 6.2 Racha (Georgia), 1999 M 7.4 Kocaeli, and M 7.2 Düzce (Turkey), and other Turkish earthquake data. Table 2 lists all the events in the dataset with relevant information on their moment magnitude, focal depth, epicenter coordinates, faulting mechanism, and breakdown of record numbers from each event. This dataset is restricted to free-field motions and inland earthquakes (except for one earthquake from the Gulf of California). A total of 47 earthquakes were selected, and can be summarized as follows: 32 earthquakes from California; six earthquakes from Turkey; four earthquakes from Taiwan and Italy; three earthquakes from Armenia, Georgia, and Uzbekistan; and two earthquakes from Alaska and Nevada. Thus, $\sim 70\%$ of the earthquakes used in our dataset are from California.

Table 2
Earthquakes Used for Updating the Graizer–Kalkan (GK15) GMPE

No	Event	Date	Style of Faulting	Moment Magnitude	Depth (km)	Epicenter Coordinates		Number of Data	Distance Range (km)
						Latitude (°)	Longitude (°)		
1	Adana-Ceyhan (Turkey)	1998	Strike-slip	6.3	18.0	36.850	35.550	4	28.0–96.0
2	Anza	2005	Strike-slip	5.2	14.2	33.529	–116.573	279	4.8–197.6
3	Big Bear City	2003	Strike-slip	4.9	6.3	34.310	–116.848	178	8.6–166.7
4	Bingol (Turkey)	2003	Strike-slip	6.4	6.0	38.940	40.510	1	6.1
5	Bishop (Rnd. Val.)	1984	Strike-slip	5.8	9.0	37.460	–118.590	1	21.9
6	Borrego Mountain	1968	Strike-slip	6.6	8.0	33.190	–116.142	5	45.7–222.4
7	Chalfant Valley	1986	Strike-slip	5.8	6.7	37.577	–118.449	5	6.4–24.5
8	Chi-Chi (Taiwan)	1999	Reverse	7.6	16.0	23.860	120.800	420	0.3–172.2
9	Coalinga-01	1983	Reverse	6.4	4.6	36.233	–120.310	46	8.4–55.8
10	Coalinga-05	1983	Reverse	5.8	7.4	36.241	77.191	11	4.6–16.2
11	Coyote Lake	1979	Strike-slip	5.7	9.6	37.085	–121.505	10	3.1–33.8
12	Denali (Alaska)	2002	Strike-slip	7.9	4.9	63.538	–147.444	24	2.7–275.9
13	Dinar (Turkey)	1995	Normal	6.4	5.0	38.110	30.050	2	3.0–39.6
14	Düzce (Turkey)	1999	Strike-slip	7.2	10.0	40.740	31.210	23	0.2–188.7
15	Erzincan (Turkey)	1992	Strike-slip	6.9	9.0	39.720	39.630	2	5.0–65.0
16	Friuli (Italy)	1976	Reverse	6.5	5.1	46.345	13.240	5	15.8–102.2
17	Gazli (Uzbekistan)	1976	Reverse	6.8	10.0	40.381	63.472	1	5.0
18	Racha (Georgia, USSR)	1991	Reverse	6.2	9.0	42.461	44.009	8	37.0–155.0
19	Gulf of California	2001	Strike-slip	5.7	10.0	32.037	–114.906	12	76.7–134.1
20	Hector Mine	1999	Strike-slip	7.1	5.0	34.574	–116.291	213	10.7–259.3
21	Imperial Valley	1979	Strike-slip	6.5	10.0	32.644	–115.309	33	0.1–50.1
22	Kocaeli (Turkey)	1999	Strike-slip	7.4	15.0	40.727	29.990	31	3.2–349.6
23	Landers	1992	Strike-slip	7.3	7.0	34.200	–116.430	69	2.2–190.1
24	Lazio-Abruzzo (Italy)	1984	Normal	5.8	14.0	41.710	13.902	5	18.9–51.3
25	Little Skul Mountain (Nevada)	1992	Normal	5.7	12.0	36.720	–116.286	8	16.1–100.2
26	Livermore	1980	Strike-slip	5.8	12.0	37.855	–121.816	7	16.7–56.1
27	Loma Prieta	1989	Reverse/strike	6.9	17.5	37.041	–121.883	82	3.9–117.1
28	Mammoth Lakes-02	1980	Strike-slip	5.7	14.0	37.628	–118.927	3	9.1–16.9
29	Mammoth Lakes-03	1980	Strike-slip	5.9	16.0	37.561	–118.831	4	5.9–11.5
30	Mammoth Lakes-04	1980	Strike-slip	5.7	5.0	37.625	–118.859	4	2.8–14.2
31	Mammoth Lakes-06	1980	Strike-slip	5.9	14.0	37.506	–118.856	5	12.0–46.5
32	Manjil (Iran)	1990	Strike-slip	7.4	19.0	36.810	49.353	7	12.6–174.6
33	Morgan Hill	1984	Strike-slip	6.2	8.5	37.306	–121.695	28	0.5–70.9
34	Northridge	1994	Reverse	6.7	17.5	34.206	–118.554	174	4.0–78.1
35	North Palm Springs	1986	Strike-slip/thrust	6.1	11.0	34.000	–116.612	32	8.6–268.0
36	Parkfield	1966	Strike-slip	6.2	10.0	35.955	–120.498	6	6.3–63.3
37	Parkfield	2004	Strike-slip	6.0	8.8	35.819	–120.364	94	0.3–169.6
38	San Fernando	1971	Reverse	6.6	13.0	34.440	–118.410	44	1.8–218.8
39	San Simeon	2003	Reverse	6.5	7.1	35.702	–121.108	138	12.4–317.8
40	Santa Barbara	1978	Thrust	5.9	12.7	34.399	–119.681	2	12.2–27.4
41	Sierra Madre	1991	Reverse	5.6	12.0	34.259	–118.001	9	10.4–48.2
42	Spitak (Armenia)	1988	Reverse	6.8	5.0	40.987	44.185	1	25.0
43	Superstition Hills-02	1987	Strike-slip	6.5	9.0	33.022	–115.831	11	1.0–27.0
44	Taiwan, Smart(5)	1981	Reverse	5.9	11.1	24.429	121.896	7	28.7–32.0
45	Whittier Narrows	1987	Reverse	6.0	14.6	34.049	–118.081	116	14.5–103.9
46	Yountville	2000	Strike-slip	5.0	10.1	38.379	–122.413	25	9.9–95.7
47	Yucaipa	2005	Reverse	4.9	11.6	34.058	–117.011	388	2.6–160.1
								Total = 2583	

These events were also used in the development of the GK07-09 model (Graizer and Kalkan, 2007, 2009). Data sources are provided in Graizer and Kalkan (2015).

Among 2583 ground-motion recordings, 1450 are from reverse-fault events, 1120 are from strike-slip fault events, and 13 are from normal-fault events. The distributions of data with respect to M and V_{S30} against the closest distance to fault rupture plane (R) are shown in Figure 1. The current dataset includes data recorded within 0.2–250 km of the

earthquake faults from events in the 4.9–7.9 magnitude range. The data used in the analysis represent main-shocks only.

Approximately half of the stations in our dataset have measured V_{S30} values, and the rest are inferred using surface geology (e.g., Wills *et al.*, 2000). The V_{S30} values range

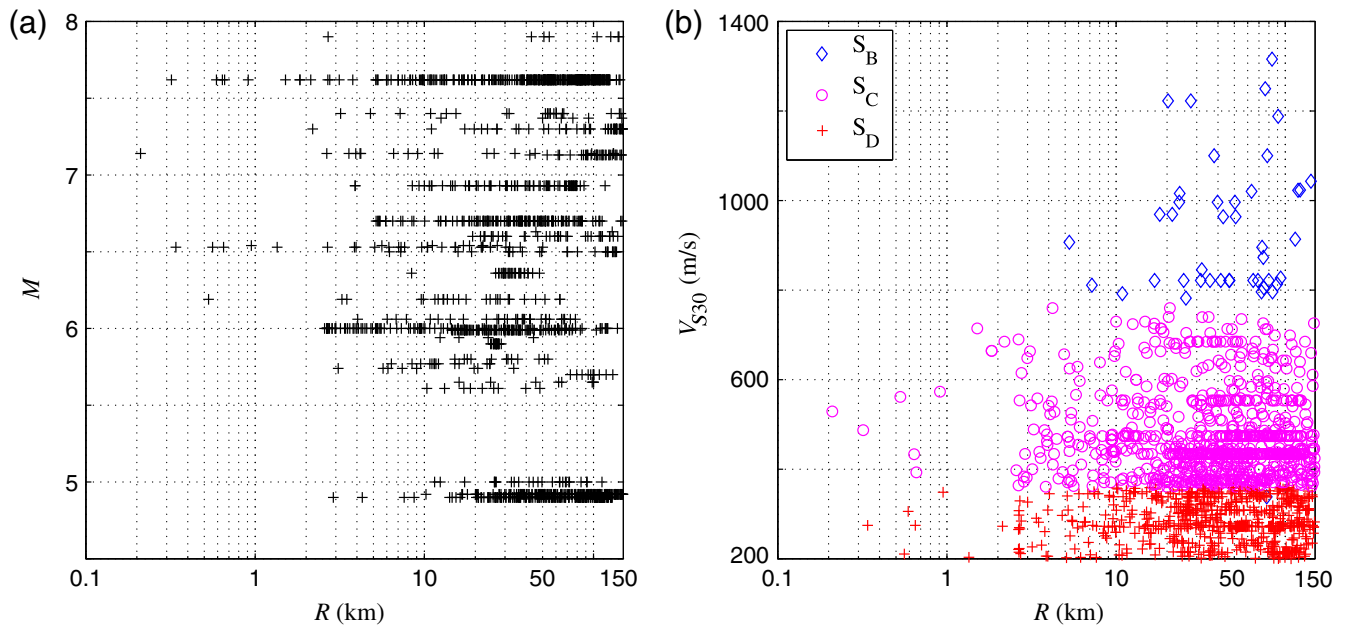


Figure 1. Earthquake data distribution with respect to (a) moment magnitude (M), and (b) shear-wave velocity in the upper 30 m of the geological profile (V_{S30}) against closest distance to fault rupture plane (R). Diamond, circle, and plus markers show National Earthquake Hazard Reduction Program (NEHRP) site categories S_B , S_C , and S_D , respectively. The color version of this figure is available only in the electronic edition.

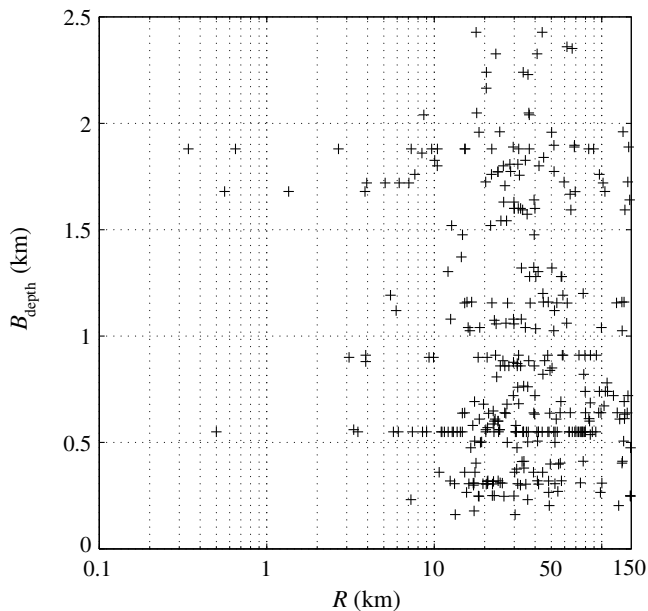


Figure 2. Earthquake data distribution with respect to closest distance to fault rupture plane (R) and basin depth (B_{depth}).

between 200 and 1316 m/s. In Figure 1b, ground-motion data are sorted according to the National Earthquake Hazard Reduction Program (NEHRP) site categories—the range of V_{S30} values in meters per second in NEHRP site categories are S_B (rock): $762 < V_{S30} < 1524$, S_C (very dense soil and soft rock): $366 < V_{S30} < 762$, and S_D (stiff soil): $183 < V_{S30} < 366$. In Figure 2, the values of depth to 1.5 km/s shear-wave velocity isosurface (B_{depth}) are plotted

against R ; B_{depth} is available for only 353 recordings in our dataset. The distribution of PGA values with respect to M and R are plotted in Figure 3; except for a handful of recordings, the values of PGA are less than about 0.8g.

It should be noted that the NGA-West2 database (see [Data and Resources](#)) was not used because it was not available to us at the time of this research.

Updated GMPE

In the following, we first introduce the final functional forms of the updated Graizer–Kalkan GMPE for PGA and spectral shape, and then explain their updates in detail.

GMPE for Peak Ground Acceleration

The updated ground-motion prediction model for PGA has 12 estimator coefficients, and six independent predictor parameters: M , moment magnitude; R , closest distance to fault rupture plane in kilometers (R , R_{rup} as in [Campbell and Bozorgnia, 2008](#)); V_{S30} , average shear-wave velocity in the upper 30 m of the geological profile in m/s; F , style of faulting, Q_0 , regional quality factor; and B_{depth} = basin depth under the site in kilometers.

The updates include the following: (1) a new anelastic attenuation term as a function of quality factor, (2) a new frequency-dependent basin-scaling term as a function of depth to the 1.5 km/s shear-wave velocity isosurface ($Z_{1.5}$), and (3) updated estimator coefficients.

The form of the prediction equation for PGA has a series of functions in a multiplication form:

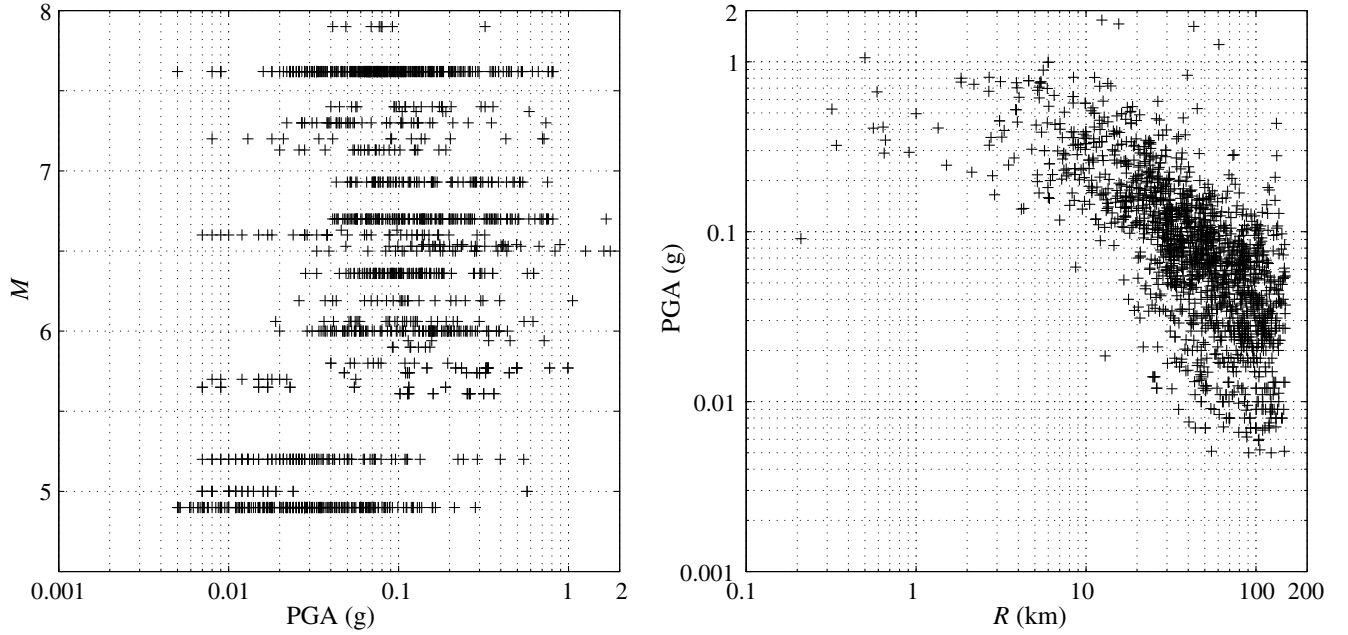


Figure 3. Horizontal peak ground acceleration (PGA) distribution with respect to moment magnitude (M), and closest distance to fault rupture plane (R).

$$\text{PGA} = \begin{matrix} G_1 \\ \text{(Magnitude and style of faulting scaling)} \\ \times \\ G_2 \\ \text{(Distance attenuation)} \\ \times \\ G_3 \\ \text{(Anelastic attenuation)} \\ \times \\ G_4 \\ \text{(Site correction)} \\ \times \\ G_5 \\ \text{(Basin effect)} \end{matrix}, \quad (1)$$

in which G_1 is a scaling function for magnitude and style of faulting, G_2 models the ground-motion distance attenuation (path scaling), G_3 adjusts the distance attenuation rate considering regional anelastic attenuation, G_4 models the site amplification owing to shallow site conditions, and G_5 is a basin scaling function. Equation (1) can be expressed in natural logarithmic space as

$$\ln(\text{PGA}) = \ln(G_1) + \ln(G_2) + \ln(G_3) + \ln(G_4) + \ln(G_5) + \sigma_{\ln(\text{PGA})}, \quad (2)$$

in which $\sigma_{\ln(\text{PGA})}$ is the total variability. The functional forms for G_1 , G_2 , G_3 , G_4 , and G_5 are given in equations (3) through (7).

$$\ln(G_1) = \ln\{[c_1 \times \arctan(M + c_2) + c_3] \times F\}, \quad (3)$$

in which F denotes the style of faulting ($F = 1.0$ for strike slip and normal faulting, $F = 1.28$ for reverse faulting, and

$F = 1.14$ for combination of strike slip and reverse faulting), and $c_{1...3}$ are the estimator coefficients.

$$\ln(G_2) = -0.5 \times \ln[(1 - R/R_0)^2 + 4 \times (D_0)^2 \times (R/R_0)], \quad (4a)$$

with

$$R_0 = c_4 \times M + c_5, \quad (4b)$$

$$D_0 = c_6 \times \cos[c_7 \times (M + c_8)] + c_9, \quad (4c)$$

and $c_{4...9}$ are estimator coefficients. In equation (2), $\ln(G_3)$, $\ln(G_4)$, and $\ln(G_5)$ are

$$\ln(G_3) = -c_{10} \times R/Q_0, \quad (5)$$

$$\ln(G_4) = b_v \times \ln(V_{S30}/V_A), \quad (6)$$

$$\ln(G_5) = \ln(1 + A_{B\text{dist}} \times A_{B\text{depth}}), \quad (7a)$$

in which c_{10} , b_v , and V_A are the estimator coefficients, and Q_0 is the regional quality factor. $A_{B\text{depth}}$ and $A_{B\text{dist}}$ are given in equations (7b) and (7c), respectively.

$$A_{B\text{depth}} = c_{11} \times 1/\sqrt{\{1 - [c_{12}/(B_{\text{depth}} + 0.1)]^2\}^2 + 4 \times c_{13}^2 \times [1.5/(B_{\text{depth}} + 0.1)]^2}, \quad (7b)$$

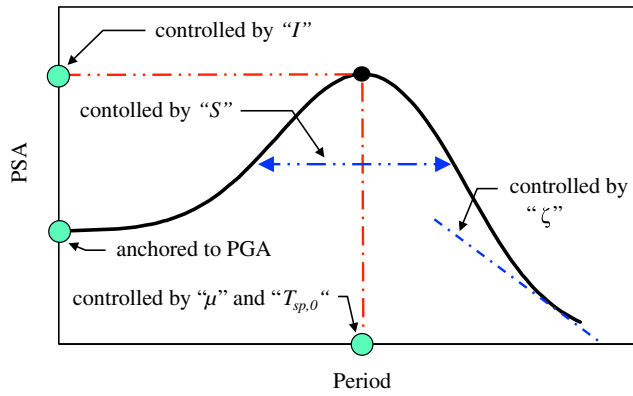


Figure 4. Generic spectral shape (PSA_{norm}) model, and its controlling parameters: I defines the peak spectral intensity, μ and $T_{sp,0}$ define the predominant period of the spectrum, S defines the wideness—area under the spectral shape—and ζ controls the decay of the spectrum at long periods depending upon basin depth. The color version of this figure is available only in the electronic edition.

The form of prediction equation for PSA is

$$PSA = PGA \times \text{spectral shape.} \tag{8}$$

The spectral shape (PSA_{norm}) is formulated as

$$PSA_{norm}(T) = I \times \exp \left[-0.5 \times \left[\frac{(\ln(T) + \mu)}{S} \right]^2 \right] + \left[\left(1 - \left(\frac{T}{T_{sp,0}} \right)^\zeta \right)^2 + 4 \times (D_{sp})^2 \times \left(\frac{T}{T_{sp,0}} \right)^\zeta \right]^{-0.5}, \tag{9a}$$

in which T is the spectral period, and D_{sp} is the estimator coefficient. As illustrated in Figure 4, I defines the peak spectral intensity, μ and $T_{sp,0}$ define the predominant period of the spectrum, S defines the spectral wideness (area under the spectral shape), and ζ controls the decay of the spectrum at long periods depending upon basin depth (B_{depth}). These functions are

$$\mu = m_1 \times R + m_2 \times M + m_3 \times V_{S30} + m_4, \tag{9b}$$

$$I = (a_1 \times M + a_2) \times \exp(a_3 \times R), \tag{9c}$$

$$S = s_1 \times R - (s_2 \times M + s_3), \tag{9d}$$

$$T_{sp,0} = \max \left\{ \begin{array}{l} 0.3 \\ |t_1 \times R + t_2 \times M + t_3 \times V_{S30} + t_4| \end{array} \right\}, \tag{9e}$$

$$\zeta = 1.763 - 0.25 \times \arctan [1.4 \times (B_{depth} - 1)], \tag{9f}$$

in which $m_{1...4}$, $a_{1...3}$, $t_{1...4}$, and $s_{1...3}$ are the estimator coefficients, and the values of which are presented in Table 3.

The estimator coefficients in Table 3 were obtained by performing regression in a number of steps, starting with a more limited dataset for constraining parameters of filter functions and proceeding to the full range similar to

A_{Bdist}

$$= 1 / \sqrt{\{1 - [c_{14}/(R + 0.1)]^2\}^2 + 4 \times c_{13}^2 \times [40/(R + 0.1)]^2}, \tag{7c}$$

in which $c_{10...14}$ are the estimator coefficients. The values of the estimator coefficients of the above equations are presented in Table 3.

GMPE for Spectral Acceleration

Similar to our previous model, the 5% damped PSA response ordinates are obtained by anchoring the spectral shape to PGA. The updated spectral shape model in GK15 has 15 coefficients and six independent predictor parameters. The independent parameters are M , R , V_{S30} , F , Q_0 , and B_{depth} . Updates on the spectral shape model include the following: (1) a modified decay term for long periods as a function of basin depth, (2) a revised term for controlling the predominant period of the response spectrum, and (3) updated coefficients.

Table 3
Estimator Coefficients of GK15

GMPE for PGA															
c_1	c_2	c_3	c_4	c_5	c_6	c_7	c_8	c_9	c_{10}	c_{11}	c_{12}	c_{13}	c_{14}	b_v	V_A
0.14	-6.25	0.37	2.237	-7.542	-0.125	1.19	-6.15	0.6	0.345	1.077	1.5	0.7	40	-0.24	484.5
Spectral Shape (PSA_{norm}) Model															
m_1	m_2	m_3	m_4	a_1	a_2	a_3	D_{sp}	t_1	t_2	t_3	t_4	s_1	s_2	s_3	
-0.0012	-0.38	0.0006	3.9	0.01686	1.2695	0.0001	0.75	0.001	0.59	-0.0005	-2.3	0.001	0.077	0.3251	

Abrahamson *et al.* (2014). However, the difference between our approach and Abrahamson *et al.* is that we did not apply smoothing on estimator coefficients because our spectral-shape prediction model is a continuous function of independent parameters.

Functions of the GK15 GMPE

The relationships between physical aspects of each filter function in equation (2) are described below.

G_1 (Magnitude and Style of Faulting)

The following scaling function models the ground-motion scaling owing to the magnitude and style of faulting:

$$G_1 = [c_1 \times \arctan(M + c_2) + c_3] \times F, \quad (10)$$

in which c_1 , c_2 , and c_3 are the estimator coefficients, and F is the style of faulting scaling term. This scaling function, empirically derived based on observations, reflects the saturation of ground-motion amplitudes with increasing magnitudes (Douglas and Jousset, 2011). According to Sadigh *et al.* (1997), reverse-fault events create ground motions approximately 28% higher than those from crustal strike-slip faults. Following this, we used $F = 1.0$ for strike-slip and normal faults, $F = 1.28$ for reverse faults, and $F = 1.14$ for combination of strike-slip and reverse faults. The G_1 and its estimation coefficients are the same as in Graizer and Kalkan (2007).

G_2 (Distance Attenuation)

One feature of our GMPE is the use of the frequency-response function in a damped single-degree-of-freedom oscillator for modeling the distance attenuation of ground motion. This modeling approach is explained in detail in Graizer and Kalkan (2007). Following this approach, the G_2 models the ground-motion distance attenuation as

$$G_2 = 1/\sqrt{(1 - R/R_0)^2 + 4 \times (D_0)^2 \times (R/R_0)}, \quad (11)$$

in which R_0 is the corner distance in the near source of an earthquake defining the plateau where the ground motion does not attenuate noticeably. In other words, R_0 defines the flat region on the attenuation curve. R_0 is directly proportional to earthquake magnitude—the larger the magnitude, the wider the plateau. The ground-motion observations show that R_0 varies from 4 km for magnitude 5 to 10 km for magnitude 7.9 (Graizer and Kalkan, 2007).

It has been observed that the largest PGA values from a given earthquake may not be recorded at the closest distance but rather at some distance from the fault, as can be seen from the records of the 1979 M 6.5 Imperial Valley earthquake, the 2004 M 6.0 Parkfield earthquake, and most recently the 2014 M 6.0 South Napa earthquake (Fig. 5). The

bump phenomenon (also called oversaturation) was recently demonstrated through modeling geometrical spreading and relative amplitudes of ground motions in eastern North America. The bump was attributed to radiation pattern effects combined with wave propagation through a 1D layered earth model (Chapman and Godbee, 2012; Baumann and Dalguer, 2014). In the case of earthquakes, this bump can be a result of one or many factors, including the aforementioned radiation pattern, directivity, and nonlinear behavior of the soil in the near source of an earthquake fault (e.g., low-velocity fault-zone-guided waves, Li and Vidale, 1996), and measuring distance as that closest to the rupture plane and not from the seismogenic (most energetic) part of the fault rupture. In equation (11), D_0 shows the damping term that designates the amplitude of the bump; $D_0 = 0.7$ results in no bump.

G_3 (Anelastic Attenuation)

The original G_3 function in the Graizer and Kalkan (2007) GMPE for PGA was a simple scaling term for far-source attenuation and basin effects. This term is now replaced with an anelastic attenuation term as

$$G_3 = \exp(-c_{10} \times R/Q_0), \quad (12)$$

in which Q_0 is the regional quality factor for propagation of seismic waves from source to site at 1 Hz, and c_{10} is the estimator coefficient. The value for Q_0 is, on average, 150 for California and 640–1000 for central and northeast United States (Singh and Herrmann, 1983; Mitchell and Hwang, 1987; Erickson *et al.*, 2004).

Figure 6a demonstrates the effects of G_3 on the PGA; the PGA data are from the 1999 M 7.6 Chi-Chi earthquake. The earlier version of the G_3 in Graizer and Kalkan (2007; hereafter referred as GK07), results in a constant attenuation rate ($R^{-1.5}$) at far-source distances (shown by dashed line). GK15 with G_3 in equation (12) are shown using $Q_0 = 75$, 150, and 300, respectively, in which a lower crustal Q_0 results in faster attenuation, and a higher Q_0 yields slower attenuation at far-source distances. Zhang and Papageorgiou (2010) estimated coda as $Q_0 = 134$ for Taiwan.

Q associated with strong motion is different from seismological measurements because the typical seismological Lg and coda wave estimates of Q sample different volumes of the crust surrounding the station and different paths than typical propagation paths of strong-motion signals (Trifunac, 1994). Trifunac demonstrated that the strong-motion Q increases from very low values near the fault ($Q = 20$ associated with the upper part of the soil profile with relatively low shear-wave velocity) to larger values at about 100–200 km away from the source associated with typical crustal attenuation. For the 2004 M 6.0 Parkfield earthquake, frequency-independent Q increased from 20 in the upper 300 m of the soil profile to higher values of 100–200 for depth range of 200–5000 m (Abercrombie, 2000).

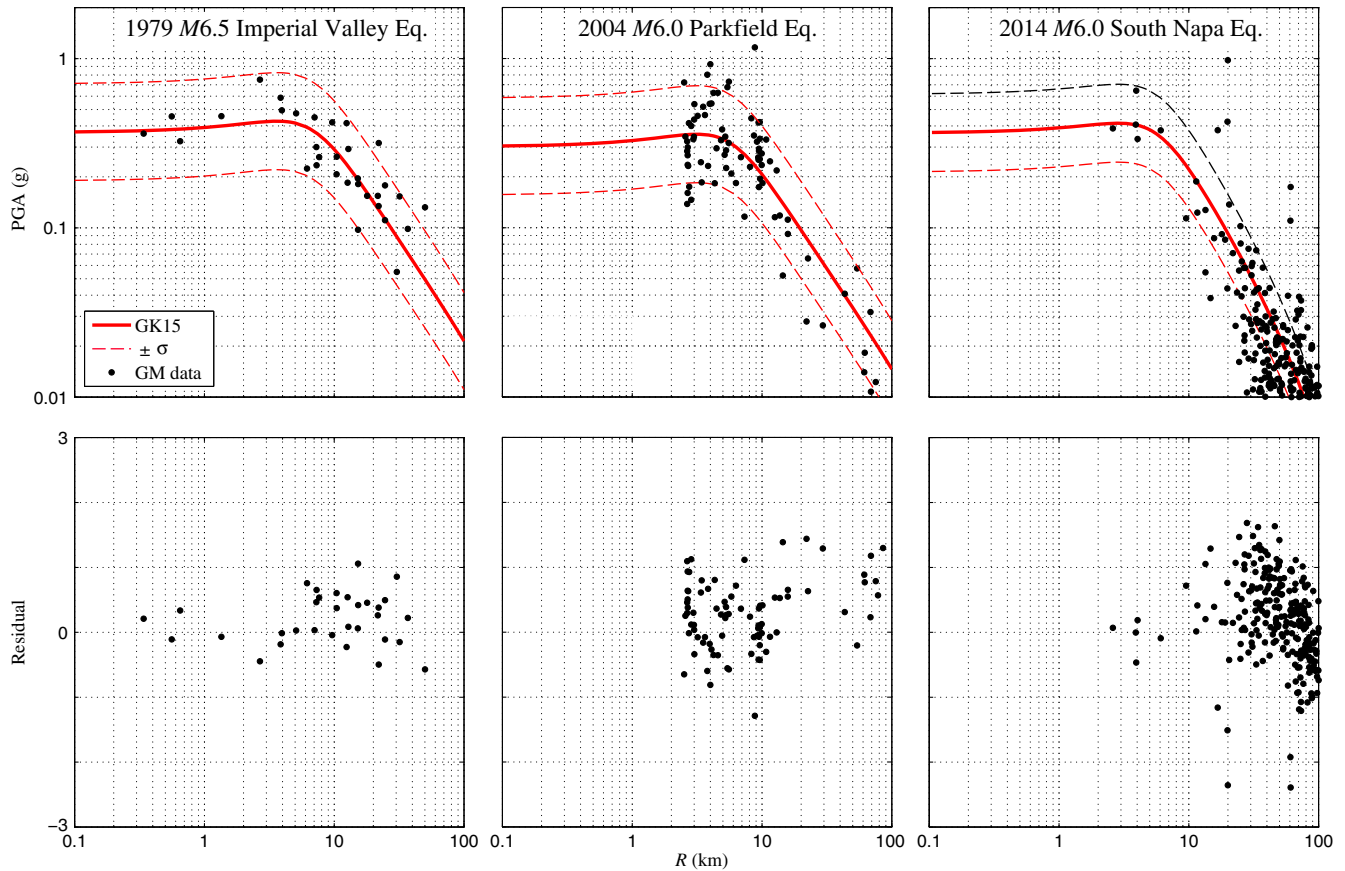


Figure 5. Ground-motion attenuation during the 1979 M 6.5 Imperial Valley, 2004 M 6.0 Parkfield and 2014 M 6.0 South Napa earthquakes. Plots show amplified PGA as a bump at near field ($R < 10$ km); this phenomenon is captured well by the Graizer–Kalkan (GK15) ground-motion prediction equation (GMPE). Ground-motion data shown are V_{S30} adjusted to 760 m/s; solid curve is for median; dashed curves are for 16th and 84th percentile of predictions; the largest PGA ($\sim 1g$) recorded at Carquinez bridge ($R = 20$ km) during the South Napa earthquake is significantly affected by local site amplification (R , closest fault distance to rupture plane; V_{S30} , shear-wave velocity in the upper 30 m of the geological profile). Residual plots show logarithmic difference between the predictions and observations. The color version of this figure is available only in the electronic edition.

Although Q may be distance dependent, Q_0 in equation (12) is a constant. In Figure 6b, we made a simple assumption that Q increases with distance from a relatively low value of 10 in the vicinity of the fault to higher values of typical Lg -type crustal Q at far-source distances ($R > 100$ km). Figure 6c compares the effects of constant $Q_0 (= 150)$ with that of the distance-dependent Q . As expected, low Q_0 in the near-source region produces slightly lower ground-motion intensity. However, this decrease does not exceed 3% at distances up to 50 km; higher Q_0 at far distances results in slower attenuation relative to the constant Q_0 . The effect of distance-dependent Q relative to the constant (distance-independent) Q_0 is not significant. Considering other uncertainties, we concluded that it is reasonable to use a constant Q_0 typical for a given region (usually that for Lg or coda waves).

In our updated GMPE for PGA, we assume a frequency-independent Q_0 . In equation (12), $c_{10} = 0.345$, based on the average value of $Q_0 = 150$ for California produces similar effects to our previous GMPE for distances of up to 200 km

(shown in Fig. 6a). The fact that Q_0 values determined using Lg or coda waves can be changed to suit the region of interest is an improvement over other GMPEs. Predictions of four NGA-West2 models and the GK15 model against the strong-motion data of the 2014 M 6.0 South Napa earthquake demonstrate that the GK15 model with lower $Q_0 = 50$ (motivated partially by the range suggested by Ford *et al.*, 2008) fits data better for this specific earthquake (Baltay and Boatwright, 2015).

G_4 (Site Correction)

Based on published studies (a list of references is given in Graizer and Kalkan, 2007), a linear site-correction filter was adopted in GK07 because of the large variability in non-linear site-correction models:

$$G_4 = \exp[b_v \times \ln(V_{S30}/V_A)]. \quad (13)$$

Equation (13) is an equivalent form of the linear site-correction formula of Boore *et al.* (1997), in which

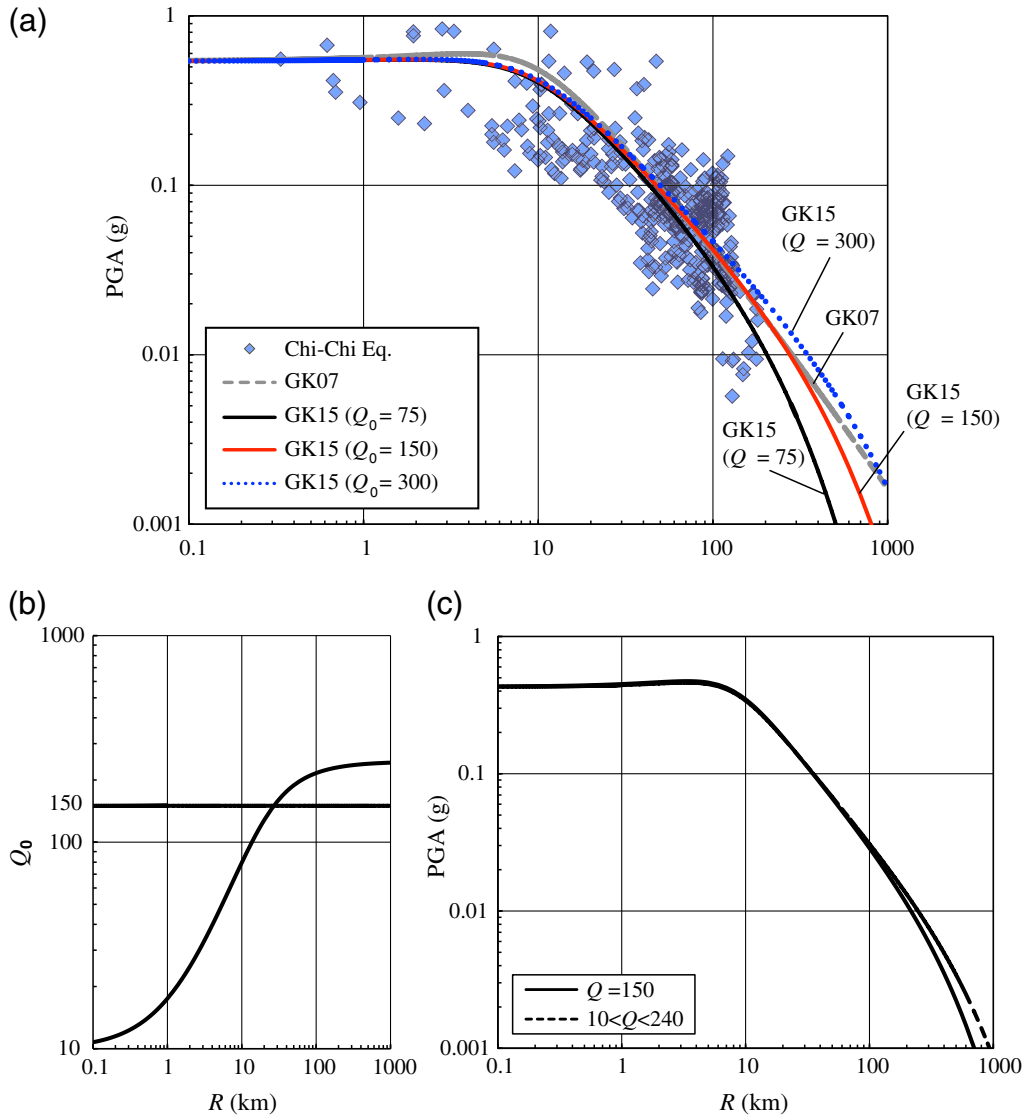


Figure 6. Model results for anelastic attenuation with constant and variable Q_0 . (a) Comparison of Graizer–Kalkan (GK07) PGA predictions with GK15 considering the 1999 M 7.6 Chi-Chi earthquake data. (b) Constant and distance-dependent Q_0 . (c) Comparison of attenuation curves with constant and distance-dependent Q_0 for an M 7.0 event ($V_{S30} = 400$ m/s) (R = closest fault distance to rupture plane). The color version of this figure is available only in the electronic edition.

$b_v = -0.371$, whereas our estimates yield $b_v = -0.24$. Equation (13), with its parameters given in Table 3, is similar to the equation of Field (2000) in exhibiting less amplification as V_{S30} decreases than that of Boore *et al.* (1997). In our updated GMPE for PGA, there is no change in G_4 from its original version in Graizer and Kalkan (2007).

G_5 (Basin Effect)

A basin consists of alluvial deposits and sedimentary rocks that are geologically younger and have a significantly lower shear-wave velocity structure than the underlying rocks, which creates a strong interface, and can trap and amplify earthquake-induced body and surface waves (Hanks, 1975; Lee *et al.*, 1995; Campbell, 1997; Frankel *et al.*,

2001). Our new basin scaling function considers combined effects of amplification in both shear and surface waves owing to basin depth under the site according to Hruby and Beresnev (2003) and Day *et al.* (2008). For simplicity, other parameters, such as the basin shape and distance to the basin edge (Joyner, 2000; Semblat *et al.*, 2002; Choi *et al.*, 2005), are not accounted for, and only the basin depth is used as a predictor parameter in our GMPE.

The mechanisms and results of shear and surface-wave amplifications in the basin are different. The basin amplification of S waves affects mostly frequencies less than ~ 10 Hz (Hruby and Beresnev, 2003), and basin amplification of surface waves affects a range of spectral frequencies from PGA to long spectral periods. During the 1992 M 7.3 Landers, 1999 M 7.1 Hector Mine, and 2010 M 7.2 El

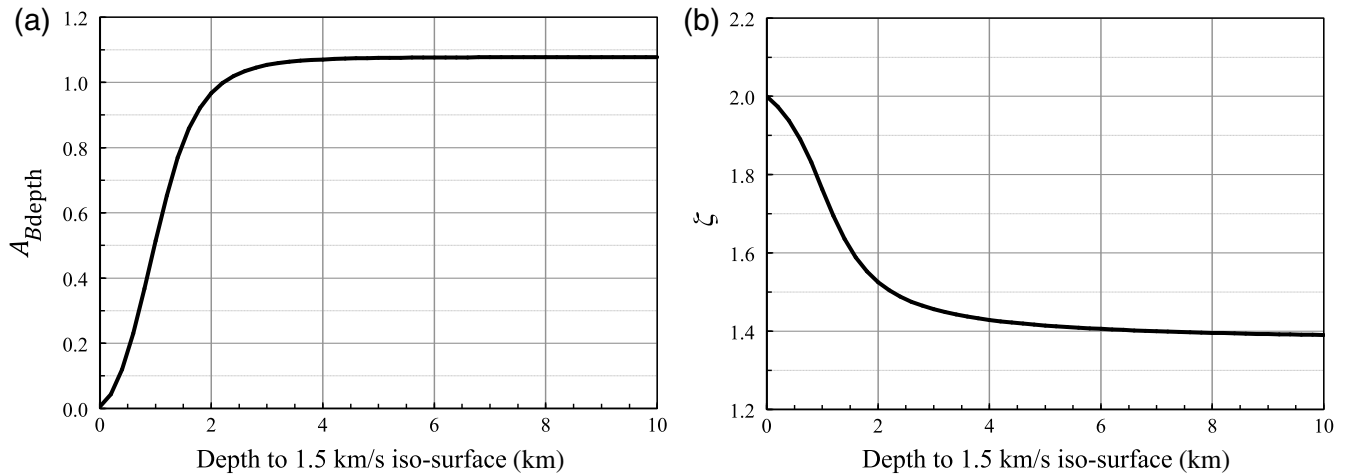


Figure 7. (a) Dependence of amplitude on basin depth (B_{depth}), and (b) dependence of the response spectrum long period decay term (ζ) on basin depth.

Mayor–Cucapah earthquakes, the PGA values observed in Los Angeles and San Bernardino basins were much higher than those measured at rock sites owing to amplified surface waves (Graizer *et al.*, 2002; Graves and Aagaard, 2011; Hatayama and Kalkan, 2012).

In our previous GMPE (Graizer and Kalkan, 2009), the spectral shape decayed at long periods with a slope of $T^{-1.5}$, averaging basin, and nonbasin effects. We change this by implementing the following basin scaling filter, which is a function of depth to the 1.5 km/s shear-wave velocity isosurface $Z_{1.5}(B_{\text{depth}})$, R , and T :

$$G_5 = 1 + A_{B_{\text{dist}}} \times A_{B_{\text{depth}}}. \quad (14)$$

$A_{B_{\text{depth}}}$ defines the amplitude of the basin effect depending upon B_{depth} . The parameters of $A_{B_{\text{dist}}}$ and $A_{B_{\text{depth}}}$ were constrained by regression according to the 1999 M 7.1 Hector Mine, 1992 M 7.3 Landers, and 1989 M 6.9 Loma Prieta earthquakes using only ground-motion data with known B_{depth} values.

As shown in Figure 7a, $A_{B_{\text{depth}}}$ varies from 0 for a nonbasin site to 1.077 for a site in a deep basin, and it saturates for basins deeper than 3 km. When $B_{\text{depth}} = 0$, $A_{B_{\text{depth}}}$ becomes negligibly small, and thus $G_5 = 1.0$ does not have any effect on ground-motion prediction. Our approach on modeling the basin effect is based on the 3D simulations of Day *et al.* (2008) who found that depth to the 1.5 km/s S -wave velocity isosurface is an appropriate parameter for use in GMPEs. Similar basin amplification was observed for the 1994 M 6.7 Northridge and 1987 M 6.0 Whittier Narrows earthquakes by Hruby and Beresnev (2003), and for the 2010 M 7.2 El-Mayor–Cucapah earthquake by Hatayama and Kalkan (2012). Our dependence of period amplification on $Z_{1.5}$ approximates the period dependence in table 3 of Hruby and Beresnev (2003).

The parameter controlling the decay rate of the spectrum at long periods (ζ in equation 9f) varies over the range of

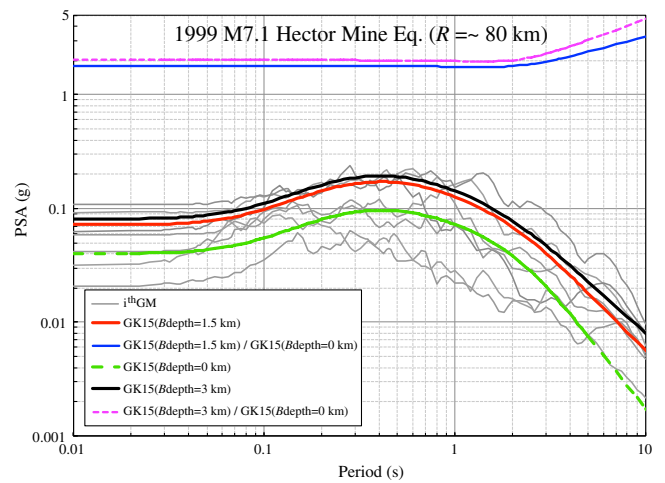


Figure 8. Comparison of pseudospectral acceleration (PSA) response computed using updated Graizer–Kalkan GMPE (GK15) for three cases: nonbasin, basin with 1.5 km depth, and basin with 3 km depth. Background data are from the 1999 M 7.1 Hector Mine earthquake at about 80 km closest fault distance to the fault-rupture plane (R). Depth to basin (B_{depth}) varies from 1 to 3 km for this dataset. The predictions are shown with the same $V_{S30} = 430$ m/s—average of the stations. The deeper basin produces a response spectrum with higher amplitudes at all periods with slower decay at long periods; it affects the long periods more than the short periods. The color version of this figure is available only in the electronic edition.

1.4–2. As shown in Figure 7b, the spectral shape decays at long periods faster (T^{-2}) for nonbasin sites and slower ($T^{-1.4}$) for deep basin sites. Figure 8 compares the PSAs for two different basin depths, $B_{\text{depth}} = 1.5$ and 3 km against the case without basin ($B_{\text{depth}} = 0$). The predictions in Figure 8 are shown with the same $V_{S30} = 430$ m/s—average of the stations. The deeper basin produces a response spectrum with higher amplitudes at all periods with slower decay at long periods; it affects the long periods more than the short

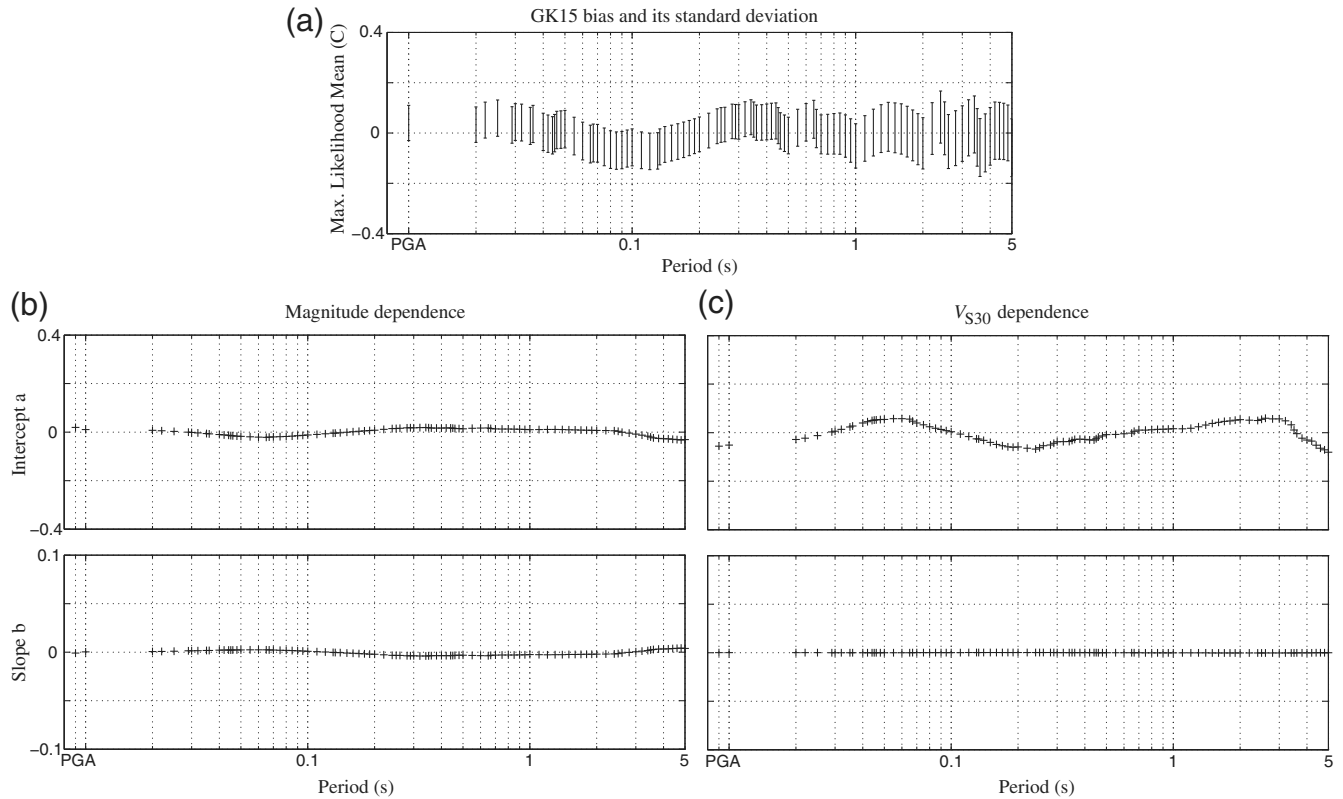


Figure 9. (a) Overall mean bias of GK15 and its standard deviation (maximum-likelihood mean C indicates the overall bias between the observations and predictions). (b) Distance, and (c) magnitude dependence of GK15 residuals. Intercept a and slope b of maximum-likelihood line fit through residuals as a function of closest fault distance to rupture plane (R).

periods. Based on a 3D modeling of ground motion, a possible explanation for the distance-dependent pattern is suggested by Olsen (2000). According to Olsen, the amplification factors are greater for events located farther from the basin edge. He suggested that the larger-amplitude surface waves generated for the distant events, in part at basin edges, are more prone to the amplification than are the predominant body waves impinging onto the basin sediments from nearby earthquakes.

Mixed-Effect Residuals Analysis

We performed a mixed-effect residuals analysis to confirm that GK15 is not biased with respect to M , R , V_{S30} , style of faulting (F), and B_{depth} by examining trends of residuals against these independent predictor parameters. The residuals at each spectral period are computed as follows:

$$\text{Res}_{ij} = \ln Y_{ij} - \mu_{ij}(M, R, V_{S30}, B_{\text{depth}}), \quad (15)$$

in which i is the event and j is the recording index, Res_{ij} is the residual of the j th recording of the i th event, and Y_{ij} is the IM (PGA or 5% damped PSA ordinates) from the j th recording of the i th event; μ_{ij} represents the GK15 median estimate in natural logarithmic units. To check for overall bias, we

used the maximum-likelihood method to recursively determine the mean of data points having the error structure of Joyner and Boore (1993), where the residuals correspond to

$$\text{Res}_{ij} = C + \eta_i + \varepsilon_{ij}, \quad (16)$$

in which C is a constant term (maximum-likelihood mean) from the mixed-effects analysis, which is a measure of the overall bias between the observations and the GMPE. The constant term (C) should be close to zero for unbiased estimates. In equation (16), η_i represents the event term (between-event residual) for event i , and ε_{ij} represents the intraevent (within-event) residual for recording j in event i . Event term η_i represents the approximate mean offset of the data for event i from the predictions provided by the median of the GMPE. Event terms (η_i) are used to evaluate the GMPE's performance relative to source predictor variables. Both event and intraevent terms are assumed to be random Gaussian variables with zero mean. Their standard deviations are indicated by τ and φ , respectively.

For each spectral period, equation (16) is solved using the maximum-likelihood formalism given in the appendix of Spudich *et al.* (1999). In Figure 9a, maximum-likelihood mean values are plotted for each spectral period ranging from

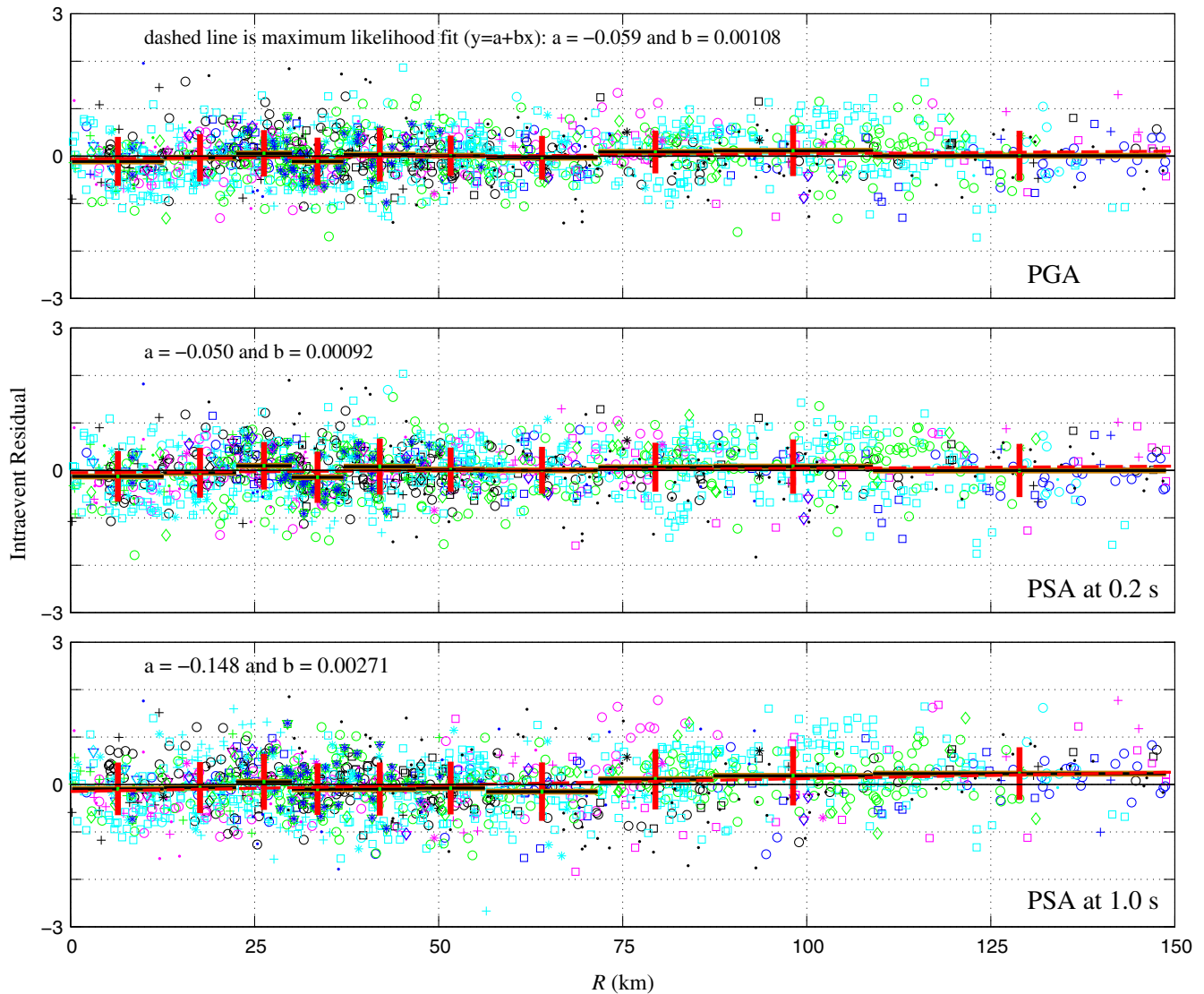


Figure 10. Distribution of intraevent residuals in natural logarithmic units for PGA and PSA at 0.2 and 1.0 s with respect to closest fault distance to rupture plane (R). Solid horizontal lines indicate size of the bins and their mean value; vertical solid lines show their standard deviation; dashed line denotes a maximum-likelihood fit to residuals; different symbols indicate different events. Note that a and b are intercept and slope of maximum-likelihood fit, respectively. The color version of this figure is available only in the electronic edition.

PGA to 5.0 s. As shown, the overall bias of GK15 is small. Some discrepancies are plausible because a continuous, smooth function of spectral period was forced to fit to all PSA data instead of a discrete data fitting at certain periods as other GMPE developers have done.

To separate interevent (between-event) disparities from intraevent (within-event) variations, we performed a mixed-effects analysis with respect to independent parameters, M , R , V_{S30} , and B_{depth} , and we fit an intercept a and slope b to residuals according to the following formulation:

$$\text{Res}_{ij} = a + bx_i + \eta_i + \varepsilon_{ij}, \quad (17)$$

in which x_i is the independent predictor parameter. Both slope and intercept computed using equation (17) are plotted against period to check for systematic bias with respect to the

independent parameters. Figure 9b,c shows distance and magnitude bias in the residuals; again both intercept and slope are near zero for all periods, indicating negligible distance dependence and no systematic magnitude bias in the residuals of GK15. We also demonstrate the same observations against the predictor parameters V_{S30} and B_{depth} , shown in Graizer and Kalkan (2015).

Intraevent (Within-Event) Residuals Analysis of Path, Site, and Basin Depth Effects

The intraevent residuals (ε_{ij}) are used to test the GK15 with respect to distance and site effects. In Figure 10, the residuals are shown in natural logarithmic units for PGA and spectral periods at 0.2 and 1.0 s, similar to Chiou and Youngs (2013); similar results for 3 s are provided in Graizer

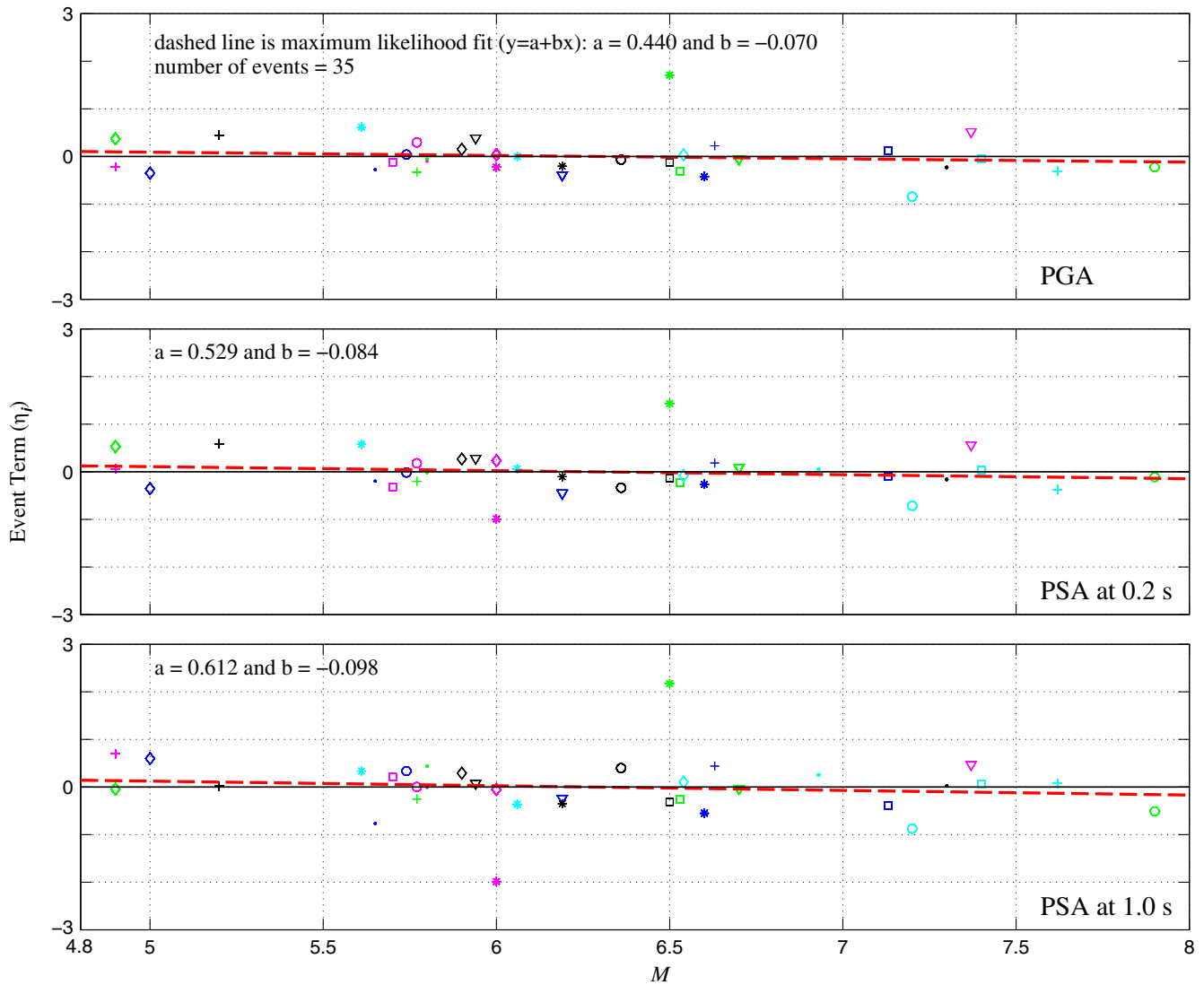


Figure 11. Distribution of event terms η_i in natural logarithmic units for PGA and PSA at 0.2 and 1.0 s with respect to moment magnitude (M); in each plot dashed line indicates a maximum-likelihood fit to all event terms; its slope and intercept are provided on top of each plot. Note that a and b are intercept and slope of maximum-likelihood fit, respectively. The color version of this figure is available only in the electronic edition.

and Kalkan (2015). We plot the intraevent residuals against R (0–150 km) using the full dataset with means and standard errors shown within bins. The bin sizes were adjusted so that each bin has approximately the same number of data points. The maximum-likelihood line is dashed, and its slope and intercept are provided on top of each plot. Although data is slightly underpredicted at 1.0 s for distances greater than 110 km, the results generally show no perceptible trend within the body of a predictor, indicating that the path-scaling functions in GK15 reasonably represent the data trends. In similar plots given in Graizer and Kalkan (2015) for V_{S30} and B_{depth} , the flatness of the trends indicates that our linear site response function (applicable for $V_{S30} > 200$ m/s) is a reasonable average for shallow crustal continental regions, and there is little dependence on B_{depth} between 1200 and

1400 m/s at 0.2 and 3.0 s—this is attributed to the scarcity of the data within this range.

Analysis of Source Effects Using Interevent (Between-Event) Residuals

Figures 11 and 12 show event terms (η_i) plotted against magnitude in the range $4.9 \leq M \leq 7.9$ and style of faulting parameter (F) considering PGA and PSA at 0.2 and 1.0 s using 35 events—the list of these events is given in table 3 of Graizer and Kalkan (2015). The majority of the events, especially at small magnitudes, are from California. The events with fewer than five recordings were excluded; this reduced the number of events from 47 to 35. Our magnitude-scaling function (G_1) captures the trends from various events as evident by near-zero intercept and near-zero slope for

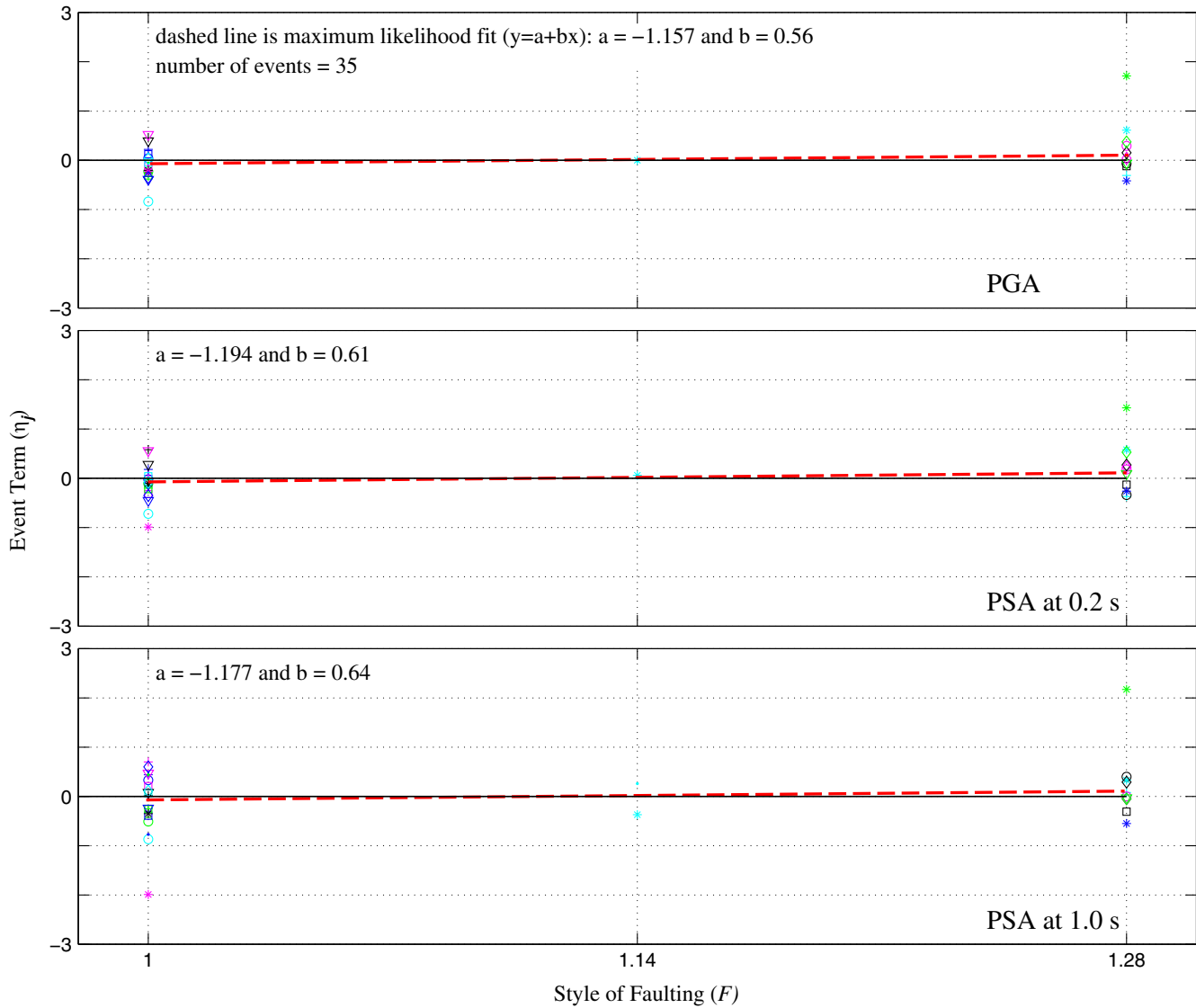


Figure 12. Distribution of event terms η_i in natural logarithmic units for PGA and PSA at 0.2 and 1.0 s with respect to style of faulting (F); in each plot dashed line indicates a maximum-likelihood fit to all event terms; its slope and intercept are provided on top of each plot. Note that a and b are intercept and slope of maximum-likelihood fit, respectively. The color version of this figure is available only in the electronic edition.

magnitude, and near-zero slope for style of faulting of the maximum-likelihood fit, indicating that there is no significant trend with either parameters or a notable offset from zero.

Terms of Standard Deviation

In GMPEs, the total residual is composed of the intraevent residual and the interevent residual. The standard deviation of total residuals (σ), that is, total aleatory variability is defined as

$$\sigma = \sqrt{\tau^2 + \phi^2}, \quad (18)$$

in which τ is the standard deviation of the interevent residuals, and ϕ of the intraevent residuals. Figure 13 plots τ , ϕ

and σ in natural logarithmic units (their values are tabulated in Table 4). The variability is larger at long periods. σ increases with period similar to the NGA-West 2 GMPEs (e.g., Abrahamson *et al.*, 2014; Boore *et al.*, 2014; Chiou and Youngs, 2014). σ is almost constant for short periods (from 0.01 to 0.3 s).

Recall that our GMPE for spectral shape is a continuous function of spectral period. To be consistent with this continuous form, we model the total aleatory variability (σ) using the method of least squares as a continuous function of spectral period (T):

$$\sigma(T) = \max \left\{ \begin{array}{l} 0.668 + 0.0047 \times \log(T) \\ 0.8 + 0.13 \times \log(T) \end{array} \right\}. \quad (19)$$

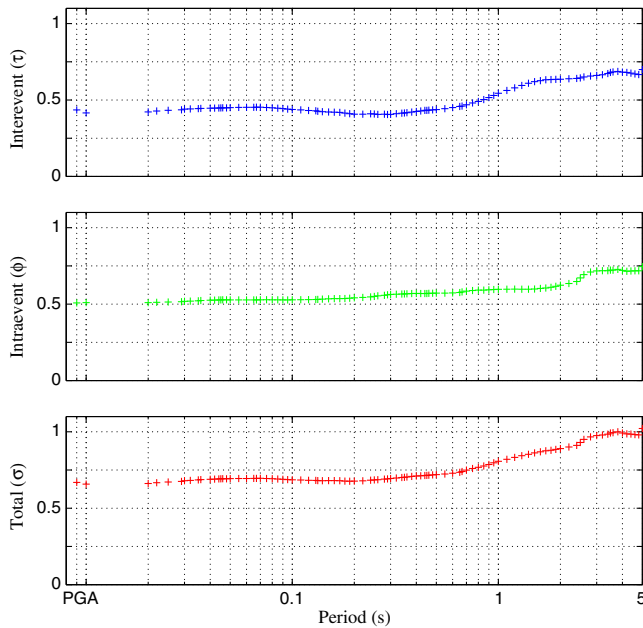


Figure 13. Interevent (between-event), intraevent (within-event), and total standard deviations of GK15 GMPE in natural-logarithmic units computed based on mixed-effects residuals analysis. The color version of this figure is available only in the electronic edition.

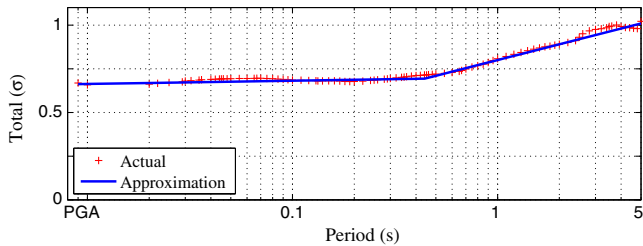


Figure 14. Total observed standard deviations (σ) of GK15 GMPE, and its parameterization via equation (19) in natural logarithmic units. The color version of this figure is available only in the electronic edition.

Figure 14 compares the parameterized σ of equation (19) with the observed σ given in Table 4, showing an excellent match at all periods. The variance analysis is conducted to examine the magnitude, distance, and V_{S30} dependence of interevent standard deviations (τ) and intraevent standard deviations (ϕ); for brevity, the results of this analysis are provided in Graizer and Kalkan (2015).

Model Results

The median PSA response spectra for GK15 is shown in Figure 15 for a vertical strike-slip earthquake scenario with $M = 5.0, 6.0, 7.0,$ and 8.0 , at distances $R = 1$ and 30 km, and $V_{S30} = 760$ and 270 m/s, similar to comparisons given in Abrahamson *et al.* (2013). Note that an increase in magnitude shifts the predominant period of spectrum to larger

Table 4

Interevent (τ), Intraevent (ϕ), and Total Standard (σ) Deviations in Natural Logarithmic Units

Period (s)	τ	ϕ	σ	Period (s)	τ	ϕ	σ
PGA	0.435	0.508	0.669	0.350	0.415	0.567	0.702
0.010	0.416	0.510	0.658	0.360	0.417	0.568	0.704
0.020	0.422	0.510	0.662	0.380	0.421	0.569	0.708
0.022	0.428	0.512	0.667	0.400	0.425	0.570	0.711
0.025	0.432	0.514	0.671	0.420	0.428	0.569	0.712
0.029	0.436	0.516	0.675	0.440	0.432	0.569	0.714
0.030	0.440	0.518	0.680	0.450	0.432	0.570	0.715
0.032	0.442	0.520	0.682	0.460	0.433	0.571	0.716
0.035	0.444	0.522	0.685	0.480	0.435	0.571	0.718
0.036	0.445	0.524	0.687	0.500	0.437	0.572	0.720
0.040	0.446	0.525	0.689	0.550	0.443	0.572	0.724
0.042	0.447	0.526	0.691	0.600	0.450	0.573	0.729
0.044	0.448	0.527	0.692	0.650	0.457	0.576	0.735
0.045	0.448	0.528	0.692	0.667	0.460	0.580	0.740
0.046	0.449	0.528	0.693	0.700	0.468	0.585	0.749
0.048	0.448	0.528	0.693	0.750	0.480	0.589	0.760
0.050	0.450	0.528	0.693	0.800	0.490	0.591	0.768
0.055	0.451	0.528	0.694	0.850	0.502	0.592	0.776
0.060	0.452	0.527	0.694	0.900	0.515	0.593	0.786
0.065	0.452	0.527	0.695	0.950	0.530	0.596	0.797
0.067	0.453	0.528	0.695	1.000	0.543	0.597	0.807
0.070	0.453	0.528	0.696	1.100	0.562	0.598	0.820
0.075	0.451	0.528	0.695	1.200	0.579	0.598	0.833
0.080	0.449	0.528	0.693	1.300	0.595	0.598	0.844
0.085	0.446	0.528	0.691	1.400	0.609	0.597	0.853
0.090	0.443	0.528	0.689	1.500	0.620	0.599	0.862
0.095	0.440	0.527	0.687	1.600	0.626	0.603	0.869
0.100	0.438	0.528	0.686	1.700	0.632	0.606	0.876
0.110	0.435	0.528	0.685	1.800	0.633	0.610	0.879
0.120	0.431	0.529	0.683	1.900	0.635	0.616	0.885
0.130	0.429	0.530	0.682	2.000	0.635	0.624	0.890
0.133	0.426	0.531	0.680	2.200	0.639	0.634	0.900
0.140	0.423	0.532	0.680	2.400	0.640	0.648	0.911
0.150	0.422	0.534	0.681	2.500	0.644	0.671	0.930
0.160	0.420	0.536	0.681	2.600	0.650	0.693	0.950
0.170	0.419	0.536	0.680	2.800	0.656	0.710	0.967
0.180	0.414	0.536	0.678	3.000	0.660	0.718	0.975
0.190	0.410	0.539	0.677	3.200	0.665	0.719	0.979
0.200	0.407	0.541	0.677	3.400	0.673	0.719	0.984
0.220	0.407	0.544	0.679	3.500	0.680	0.723	0.992
0.240	0.409	0.547	0.683	3.600	0.683	0.722	0.994
0.250	0.408	0.550	0.685	3.800	0.687	0.727	1.000
0.260	0.406	0.554	0.687	4.000	0.682	0.721	0.992
0.280	0.407	0.558	0.690	4.200	0.680	0.715	0.986
0.290	0.405	0.561	0.692	4.400	0.676	0.717	0.985
0.300	0.406	0.564	0.694	4.600	0.670	0.718	0.982
0.320	0.410	0.565	0.698	4.800	0.667	0.718	0.980
0.340	0.414	0.566	0.701	5.000	0.699	0.745	1.022

values (see fig. 3 of Graizer and Kalkan, 2009). The predominant period in our spectral shape model is controlled by μ and $T_{sp,0}$ shown in Figure 4, and both of which are magnitude dependent.

The path scaling, shown in Figure 16 for PGA and spectral periods at 0.2, 1.0, and 3.0 s, gives the median ground motion from strike-slip earthquakes on a soft-rock site condition ($V_{S30} = 760$ m/s) for four different magnitudes,

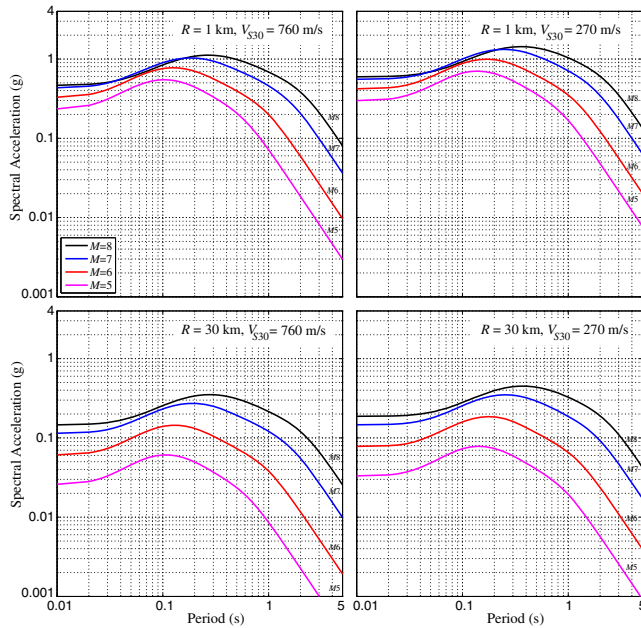


Figure 15. Comparison of median PSA for strike-slip magnitude (M) 5.0, 6.0, 7.0, and 8.0 earthquakes at $R = 1$ and 30 km and $V_{S30} = 270$ and 760 m/s considering $Q_0 = 150$ and $B_{\text{depth}} = 0$ km (R , closest fault distance to rupture plane; V_{S30} , shear-wave velocity in the upper 30 m of the geological profile; Q_0 , quality factor; B_{depth} , depth to basin). The color version of this figure is available only in the electronic edition.

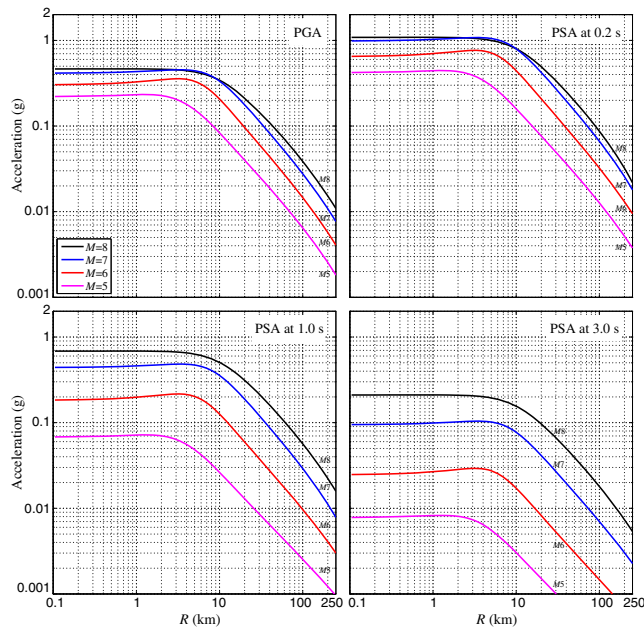


Figure 16. Comparison of distance scaling for strike-slip magnitude (M) 5.0, 6.0, 7.0, and 8.0 earthquakes at median PGA and PSA at 0.2, 1.0, and 3.0 s considering $V_{S30} = 760$ m/s, $Q_0 = 150$, and $B_{\text{depth}} = 0$ km (R , closest fault distance to rupture plane; V_{S30} , shear-wave velocity in the upper 30 m of the geological profile; Q_0 , quality factor; B_{depth} , depth to basin). At intermediate distance range (5–20 km from the fault), the GK15 produces higher acceleration values; these high accelerations look like a bump on the attenuation curves. The color version of this figure is available only in the electronic edition.

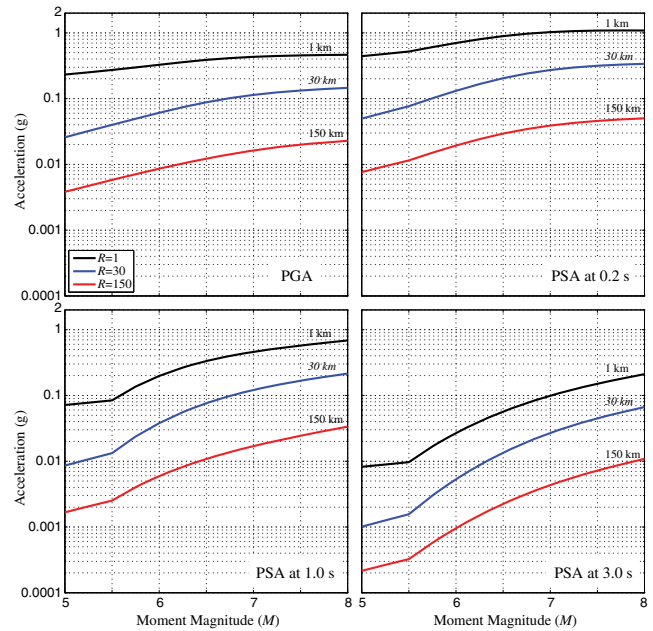


Figure 17. Comparison of magnitude scaling for strike-slip earthquakes at closest fault distance to rupture plane, $R = 1$, 30, and 150 km for median PGA and PSA at 0.2, 1.0, and 3.0 s considering $V_{S30} = 760$ m/s, $Q_0 = 150$, and $B_{\text{depth}} = 0$ km (R , closest fault distance to rupture plane; V_{S30} , shear-wave velocity in the upper 30 m of the geological profile; Q_0 , quality factor; B_{depth} , depth to basin). Note that the weak scaling of the short-period motion at short distances reflects the saturation with magnitude. The color version of this figure is available only in the electronic edition.

$M = 5.0, 6.0, 7.0,$ and 8.0 . At intermediate distance ranges (5–20 km from the fault), GK15 produces higher acceleration values than those at the closer distances, which appear as the bump on the attenuation curves (as discussed earlier in the [G₂ \(Distance Attenuation\)](#) section).

The magnitude scaling of the current model is shown in Figure 17 for vertical strike-slip earthquakes on soft-rock site conditions ($V_{S30} = 760$ m/s) for PGA, $T = 0.2, 1.0,$ and 3.0 s at distances of $R = 1, 30,$ and 150 km. The break in the magnitude scaling at $M 5.5$ is driven by consistency in response spectra of recorded data. The weak scaling of the short-period motion at short distances reflects the saturation with magnitude. Further detailed model results considering other independent parameters (e.g., V_{S30} , Q_0 , and B_{depth}) can be found in [Graizer and Kalkan \(2015\)](#).

In Figures 18 and 19, PSA predictions of GK15 are compared with those computed from near-field (0–20 km) and far-field (45–65 km) records of select major earthquakes from California, Turkey, and Taiwan. The ground-motion records either correspond to NEHRP site category C or D. For each earthquake, the number of records satisfying the distance and soil condition selection criteria is listed on each panel where the average spectra of records are shown by jagged thick curves, and they are compared with the GMPE predictions shown by smooth thick curves. Individual spectra of records shown by jagged thin curves demonstrate the aleatoric

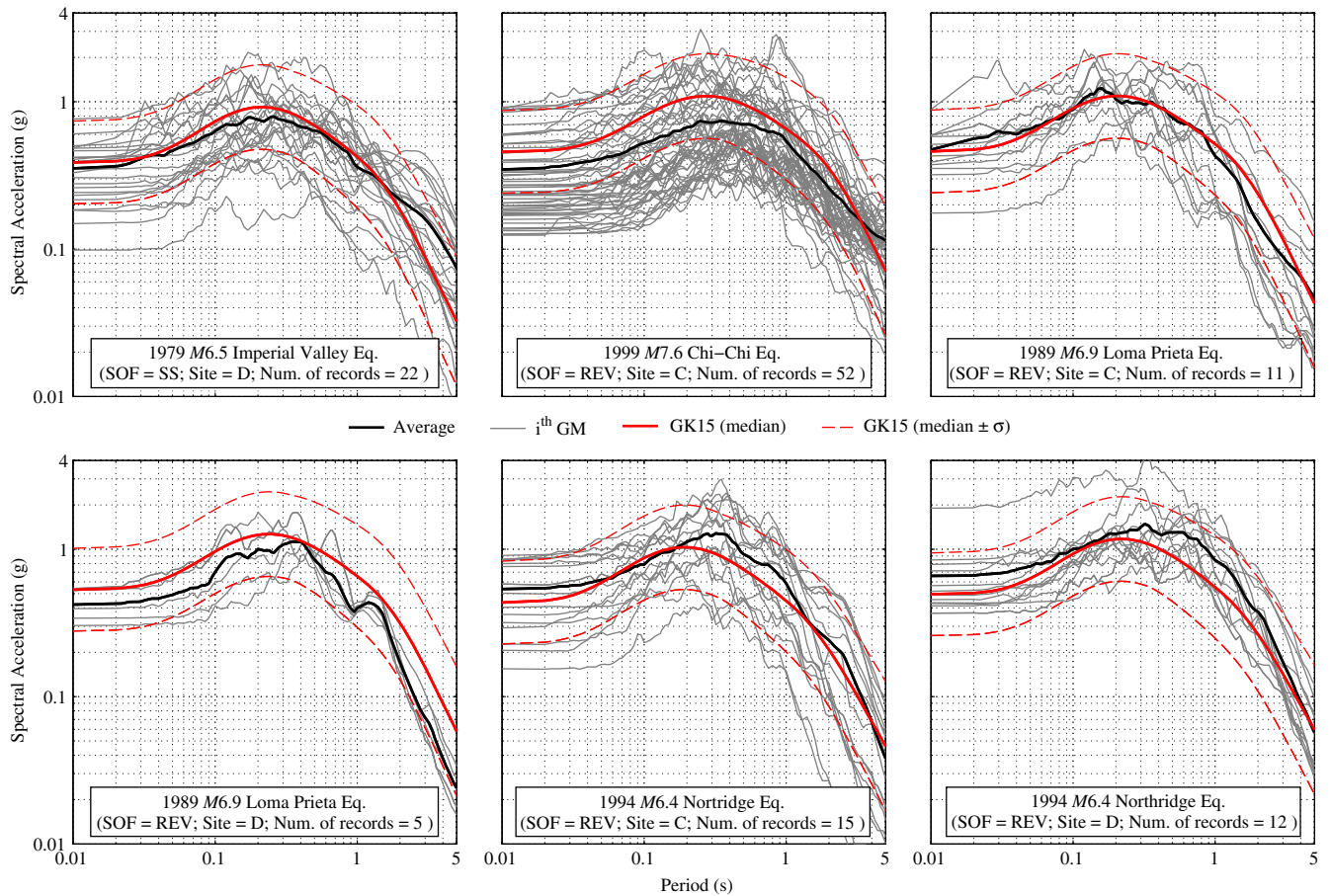


Figure 18. Comparison of GK15 predictions for PSA with the observations from select earthquakes. Ground-motion data correspond to randomly oriented horizontal components of near-field records ($R_{\text{rup}} = 10 \pm 10$ km) with NEHRP site class C or D. Dashed curves indicate 16th and 84th percentile predictions; SOF, style of faulting; SS, strike-slip fault; REV, reverse fault; number of records from each earthquake are indicated. The color version of this figure is available only in the electronic edition.

variability. The predictions from the GK15 are for the average V_{S30} of each individual dataset. As shown, the 16th and 84th percentile predictions (shown by dashed curves) bound the majority of the PSA data. For all events, the GK15 clearly results in PSA predictions closer to the average of the observations; the predicted and observed trends of the peak (period and amplitude) of the response spectra with magnitude and distance match. The width of the predicted response spectra is also comparable to the observations.

Comparisons with Select NGA-West2 Models

We compare GK15 with two NGA-West2 models of Abrahamson *et al.* (2014) (hereafter referred to as ASK14) and Boore *et al.* (2014) (hereafter referred to as BSSA14). We do not include other NGA-West2 models (Campbell and Bozorgnia, 2014; Chiou and Youngs, 2014) for simplicity and because they themselves compare well with BSSA14 and ASK14 (Gregor *et al.*, 2014). Figure 20 compares the median attenuation of PGA and PSA at 0.2 and 1.0 s for a vertically dipping strike-slip earthquake as a function of R at $V_{S30} = 760$ m/s. Our predictions are in good agreement with the predictions

of the two NGA-West2 models for the given range of magnitudes and distances. For PGA and PSA at 0.2 s, GK15 produces similar or slightly lower ground motions as compared with BSSA14 and ASK14 at close distances (0–5 km). At intermediate distances (5–20 km), GK15 produces higher values because of the bump.

The response spectra from magnitude 6.0, 7.0, and 8.0 earthquakes at $R = 1$ and 30 km from a vertically dipping strike-slip fault and $V_{S30} = 760$ m/s are shown in Figure 21. There is similarity among the three models for these cases. The observed difference between the models increases for the $M 8$ case, especially at the long spectral periods, because magnitude-scaling functions and data used to constrain them vary from one GMPE to another; it is also related to lack of observations at this magnitude range. Further comparisons with BSSA14 and ASK14 models as well as comparisons with the GK07-09 model can be found in Graizer and Kalkan (2015).

Range of Applicability

GK15 is applicable to earthquakes of moment magnitude 5.0–8.0 (except for $M > 7.0$ normal-slip events), at

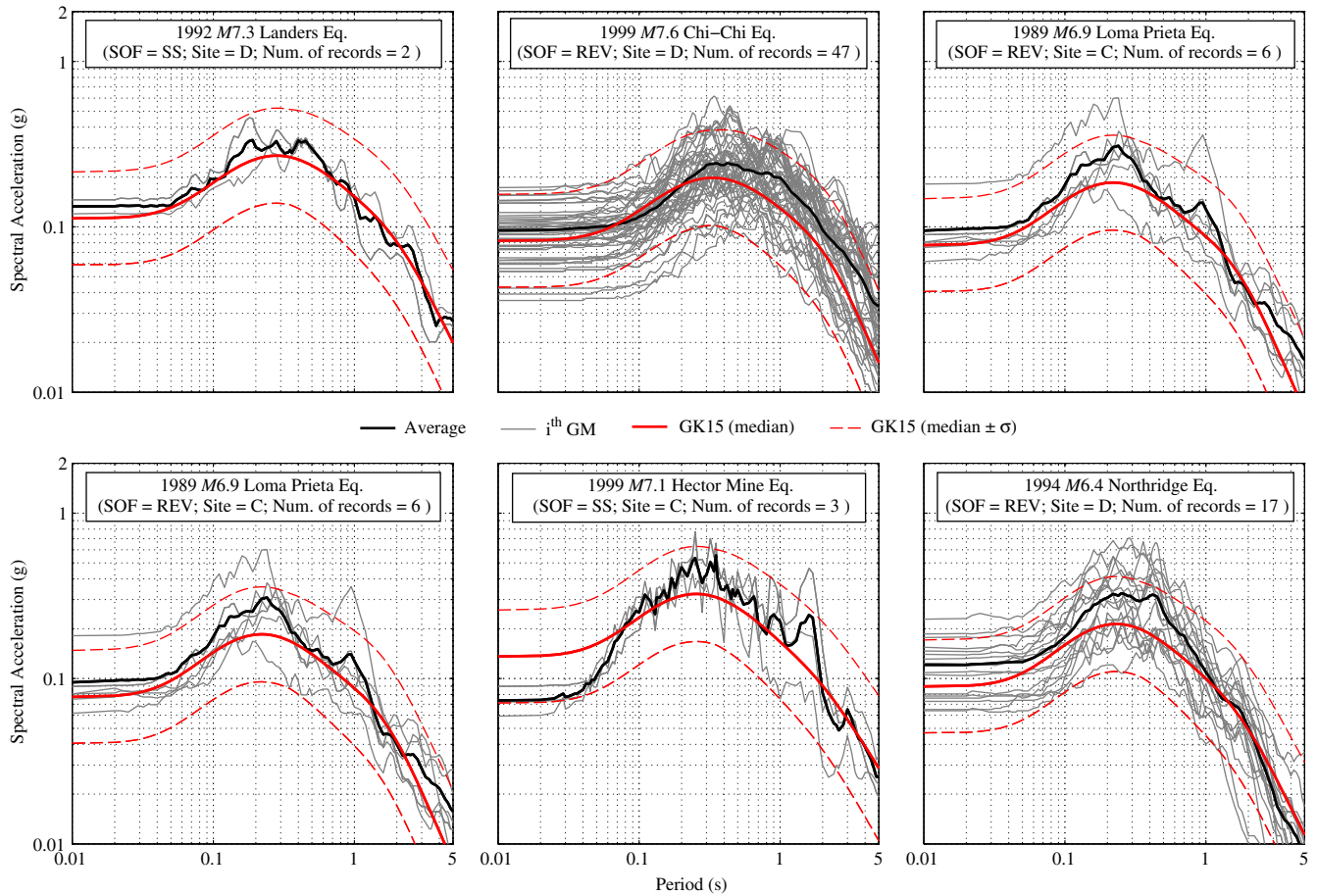


Figure 19. Comparison of GK15 predictions for PSAs with the observations from select earthquakes. Ground-motion data correspond to randomly oriented horizontal components of far-field records ($R = 55 \pm 10$ km) with NEHRP site class C or D. Dashed curves indicate 16th and 84th percentile predictions; SOF, style of faulting; SS, strike-slip fault; REV, reverse fault; number of records from each earthquake are indicated. The color version of this figure is available only in the electronic edition.

closest distances to fault rupture plane from 0 to 250 km, at sites having V_{S30} in the range from 200 to 1300 m/s, and for spectral periods (T) of 0.01–5 s. Neither hanging-wall effects nor directivity effects are explicitly modeled, but the average directivity effect is included through the variability of the data.

Summary and Discussion

In this article, the Graizer–Kalkan GMPE for PGA and 5% damped PSA response ordinates is revised to account for differences in ground-motion scaling in terms of regional far-source distance attenuation and basin effects. The new GMPE is controlled by six input predictor parameters, including moment magnitude, closest distance to the fault rupture, style of faulting, shear-wave velocity in the upper 30 m of site geological formation, regional quality factor (Q_0), and basin depth (defined as the depth to 1.5 km/s shear-wave velocity isosurface).

The revised Graizer–Kalkan GMPE (GK15) offers a much simpler functional form than the recent NGA-West2 models (e.g., ASK14; BSSA14; Campbell and Bozorgnia, 2014 [CB14]; Chiou and Youngs, 2014 [CY14]), and it has

comparable standard deviations. The GK15 models PSA as a continuous function of spectral period, whereas the NGA-West2 models use a discrete functional form to compute PSA response ordinates at certain periods only (a total of 21 periods for ASK14, CB14, and CY14, and 107 periods for BSSA14 from 0.01 to 10 s). The advantages of continuous function are that period-by-period regression analyses are eliminated, the number of estimator coefficients is minimized, and a smooth spectrum is obtained directly from the regression analysis. Because this approach is simple and provides more control, it is easier to model and constrain parameters affecting the spectral shape. The GK15's use of the quality factor (determined using Lg or coda waves) that can be changed to suit the region of interest is an improvement over other GMPEs.

Comparisons of GK15 with ASK14 and BSSA14 demonstrate that GK15 produces similar or slightly smaller ground motions at very close distances to the fault (up to about 5 km) and at distances of more than 20 km from the fault for earthquakes with a magnitude larger than 6.0. At intermediate distances (5–20 km from the fault), GK15

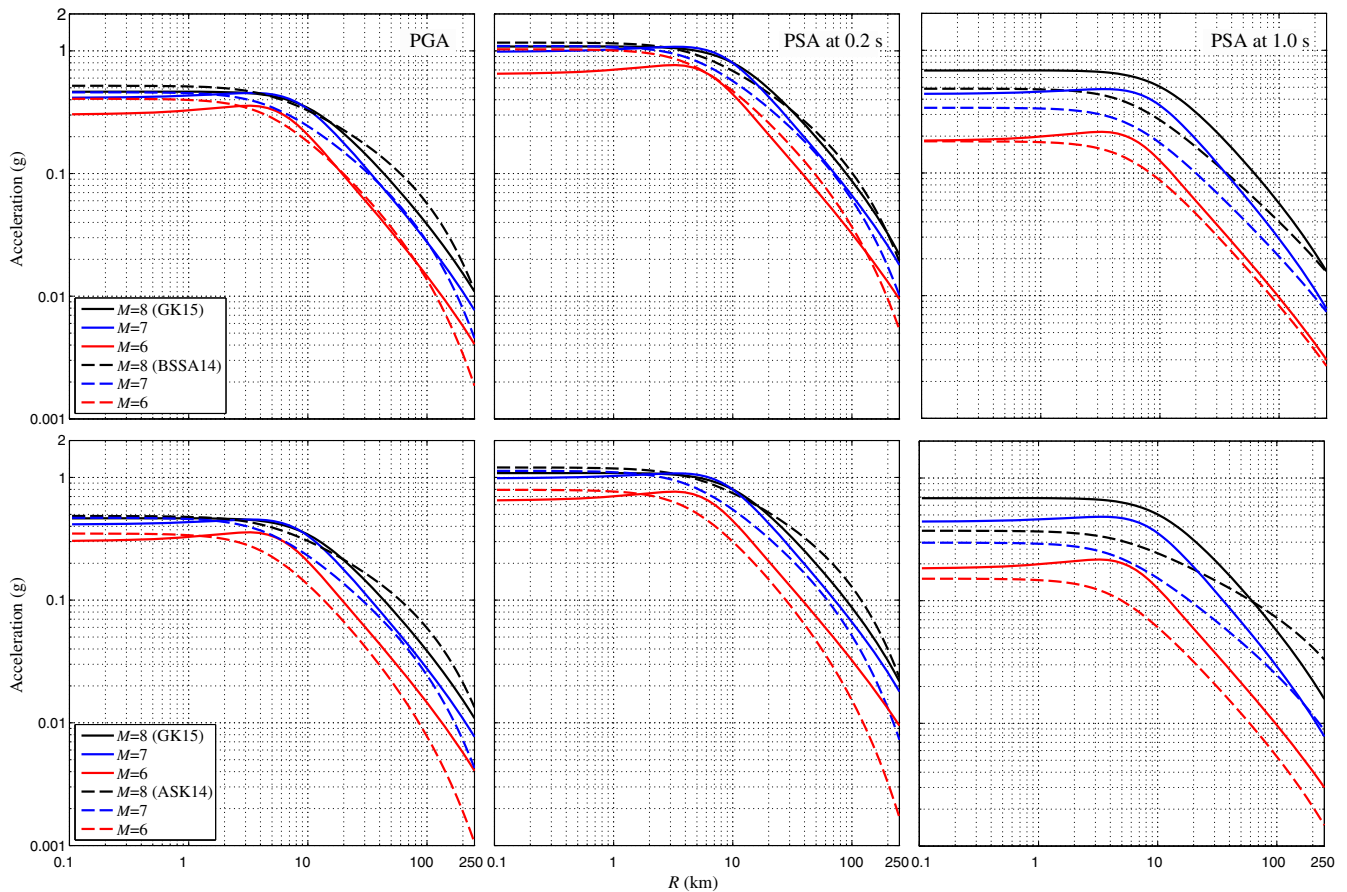


Figure 20. Comparison of distance scaling of GK15 with Boore *et al.* (2014) (BSSA14) and Abrahamson *et al.* (2014) (ASK14) for strike-slip magnitude (M) 6.0, 7.0, and 8.0 earthquakes at median PGA and PSAs at 0.2 and 1.0 s considering $V_{S30} = 760$ m/s, $Q_0 = 150$, and $B_{\text{depth}} = 0$ km (V_{S30} , shear-wave velocity in the upper 30 m of the geological profile; Q_0 , quality factor; B_{depth} , depth to basin). The color version of this figure is available only in the electronic edition.

produces higher estimates of ground motion than either ASK14 or BSSA14 does.

Compared with the GK07-09 model (Graizer and Kalkan, 2007, 2009), GK15 yields very similar PGA values whereas spectral ordinates predicted are larger at $T < 0.2$ s, and they are smaller at longer periods. This adjustment was done based on reevaluation of the ground-motion data from California earthquakes such as Landers, Northridge, and Hector Mine. The aleatory variability of GK15 is larger than that obtained in our previous model.

In conclusion, the GK15 GMPE is a significant improvement over our previous model (GK07-09), and provides a demonstrable, reliable description of ground-motion amplitudes recorded from shallow crustal earthquakes in active tectonic regions over a wide range of magnitudes, distances, and site conditions.

Data and Resources

The Graizer–Kalkan (GK15) ground-motion prediction equation (GMPE) is available in MATLAB (<http://www.mathworks.com/products/matlab/>, last accessed March 2016),

FORTRAN, and Excel at <http://earthquake.usgs.gov/research/software/> (last accessed July 2015). Also provided in this link is an example MATLAB routine to generate a site-specific response spectrum for given hazard conditions. Readers may find further details about GK15 in the U.S. Geological Survey (USGS) open-file report available at <http://pubs.usgs.gov/of/2015/1009/> (last accessed July 2015). The 2014 M 6.0 South Napa earthquake ground-motion data used here are available at <http://earthquake.usgs.gov/earthquakes/shakemap/nc/shake/72282711/#download> (last accessed July 2015). V_{S30} values at each station are taken from the Next Generation of Attenuation (NGA)-West2 database (<http://peer.berkeley.edu/ngawest2/databases/>, last accessed July 2015) or the grid.xml file also available with the ShakeMap download link provided previously.

Acknowledgments

The authors thank Martin Chapman, Jon Ake, and Dogan Seber for insightful discussions on ground-motion attenuation. Special thanks are extended to Stephen Harmsen, Nick Gregor, and Michael Pasyanos for independently testing our ground-motion prediction equation (GMPE), and providing useful feedback. David Boore, Art Frankel, Brad Aagaard, Anne-

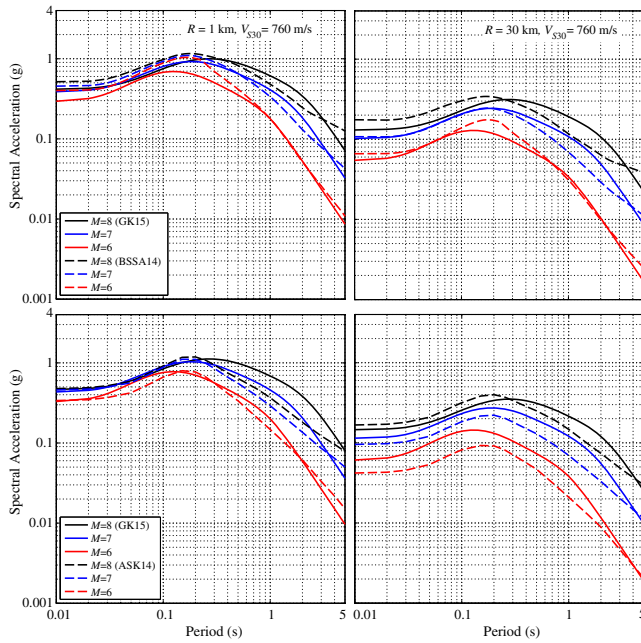


Figure 21. Comparison of spectra from GK15 with Boore *et al.* (2014) (BSSA14) and Abrahamson *et al.* (2014) (ASK14) for strike-slip magnitude (M) 6.0, 7.0, and 8.0 earthquakes at closest fault distance to rupture plane $R = 1$ and 30 km, considering $V_{S30} = 760$ m/s, $Q_0 = 150$, and $B_{\text{depth}} = 0$ km (V_{S30} = shear-wave velocity in the upper 30 m of the geological profile; Q_0 = quality factor; B_{depth} = depth to basin). The color version of this figure is available only in the electronic edition.

marie Baltay, and two anonymous reviewers have reviewed the material presented here, and offered valuable comments and suggestions, which helped improving technical quality and presentation of our work. We also thank Paul Spudich for his assistance with mixed-effects residuals analysis, and Annemarie Baltay for providing computer codes to plot Next Generation Attenuation (NGA)-West2 GMPes.

References

- Abercrombie, R. E. (2000). Crustal attenuation and site effects at Parkfield, California, *J. Geophys. Res.* **105**, no. B3, 6277–6286.
- Abrahamson, N. A., W. J. Silva, and R. Kamai (2013). Update of the AS08 ground-motion prediction equations based on the NGA-West 2 data set, *Pacific Earthq. Eng. Res. Center Rept. 2013/04*, 143 pp.
- Abrahamson, N. A., W. J. Silva, and R. Kamai (2014). Summary of the ASK14 ground motion relation for active crustal regions, *Earthq. Spectra* **30**, no. 3, 1025–1055.
- Baker, J. W. (2011). Conditional mean spectrum: Tool for ground motion selection, *J. Struct. Eng.* **137**, no. 3, 322–331.
- Baltay, A. S., and J. Boatwright (2015). Ground-motion observations of the 2014 South Napa earthquake, *Seismol. Res. Lett.* **86**, 355–360.
- Baumann, C., and L. A. Dalguer (2014). Evaluating the compatibility of dynamic rupture-based synthetic ground motion with empirical ground-motion prediction equation, *Bull. Seismol. Soc. Am.* **104**, no. 2, 634–652.
- Boore, D. M., W. B. Joyner, and T. E. Fumal (1997). Equations for estimating horizontal response spectra and peak acceleration from western North American earthquakes; a summary of recent work, *Seismol. Res. Lett.* **68**, no. 1, 128–153.
- Boore, D. M., J. P. Stewart, E. Seyhan, and G. M. Atkinson (2014). NGA-West 2 equations for predicting PGA, PGV, and 5% damped PSA for shallow crustal earthquakes, *Earthq. Spectra* **30**, no. 3, 1057–1085.
- Bozorgnia, Y., N. A. Abrahamson, L. Al Atik, T. D. Ancheta, G. M. Atkinson, J. W. Baker, A. Baltay, D. M. Boore, K. W. Campbell, B. S.-J. Chiou, *et al.* (2014). NGA-West 2 research project, *Earthq. Spectra* **30**, 973–987.
- Campbell, K. W. (1997). Empirical near-source attenuation relations for horizontal and vertical components of peak ground acceleration, peak ground velocity, and pseudo-absolute acceleration response spectra, *Seismol. Res. Lett.* **68**, no. 1, 154–179.
- Campbell, K. W., and Y. Bozorgnia (2008). NGA ground motion model for the geometric mean horizontal component of PGA, PGV, PGD and 5% damped linear elastic response spectra for periods ranging from 0.01 to 10 s, *Earthq. Spectra* **24**, no. 1, 139–171.
- Campbell, K. W., and Y. Bozorgnia (2014). NGA-West 2 ground motion model for the average horizontal components of PGA, PGV, and 5% damped linear acceleration response spectra, *Earthq. Spectra* **30**, no. 3, 1087–1115.
- Chapman, M. C., and R. W. Godbee (2012). Modeling geometrical spreading and the relative amplitudes of vertical and horizontal high-frequency ground motions in eastern North America, *Bull. Seismol. Soc. Am.* **102**, no. 5, 1957–1975.
- Chiou, B., and R. R. Youngs (2013). Update of the Chiou and Youngs NGA ground motion model for average horizontal component of peak ground motion and response spectra, *Pacific Earthq. Eng. Res. Center Rept. 2013/07*, 76 pp.
- Chiou, B., and R. R. Youngs (2014). Update of the Chiou and Youngs NGA model for the average horizontal component of peak ground motion and response spectra, *Earthq. Spectra* **30**, no. 3, 1117–1153.
- Chiou, B., R. Darragh, N. Gregor, and W. Silva (2008). NGA project strong-motion database, *Earthq. Spectra* **24**, no. 1, 23–44.
- Choi, Y., J. P. Stewart, and R. W. Graves (2005). Empirical model for basin effects accounts for basin depth and source location, *Bull. Seismol. Soc. Am.* **95**, no. 4, 1412–1427.
- Day, S. M., R. Graves, J. Bielik, D. Dreger, S. Larsen, K. B. Olsen, A. Pitarka, and L. Ramirez-Guzman (2008). Model for basin effects on long-period response spectra in southern California, *Earthq. Spectra* **24**, no. 1, 257–277.
- Douglas, J., and P. Jousset (2011). Modeling the difference in ground-motion magnitude-scaling in small and large earthquakes, *Seismol. Res. Lett.* **82**, no. 4, 504–508.
- Erickson, D., D. E. McNamara, and H. M. Benz (2004). Frequency-dependent $Lg Q$ within the continental United States, *Bull. Seismol. Soc. Am.* **94**, no. 5, 1630–1643.
- Field, E. H. (2000). A modified ground motion attenuation relationship for southern California that accounts for detailed site classification and a basin-depth effect, *Bull. Seismol. Soc. Am.* **90**, no. 6B, S209–S221.
- Ford, S. R., D. S. Dreger, K. Mayeda, W. R. Walter, L. Malagnini, and W. S. Phillips (2008). Regional attenuation in northern California; a comparison of five 1D Q methods, *Bull. Seismol. Soc. Am.* **98**, no. 4, 2033–2046.
- Frankel, A., D. Carver, E. Cranswick, T. Bice, R. Sell, and S. Hanson (2001). Observation of basin ground-motions from a dense seismic array in San Jose, California, *Bull. Seismol. Soc. Am.* **91**, no. 1, 1–12.
- Graizer, V., and E. Kalkan (2007). Ground-motion attenuation model for peak horizontal acceleration from shallow crustal earthquakes, *Earthq. Spectra* **23**, no. 3, 585–613.
- Graizer, V., and E. Kalkan (2009). Prediction of response spectral acceleration ordinates based on PGA attenuation, *Earthq. Spectra* **25**, no. 1, 39–69.
- Graizer, V., and E. Kalkan (2011). Modular filter-based approach to ground-motion attenuation modeling, *Seismol. Res. Lett.* **82**, no. 1, 21–31.
- Graizer, V., and E. Kalkan (2015). Update of the Graizer–Kalkan ground-motion prediction equations for shallow crustal continental earthquakes, *U.S. Geol. Surv. Open-File Rept. 2015-1009*, doi: [10.3133/ofr20151009](https://doi.org/10.3133/ofr20151009).
- Graizer, V., E. Kalkan, and K. W. Lin (2013). Global ground-motion prediction equation for shallow crustal regions, *Earthq. Spectra* **29**, no. 3, 777–791.

- Graizer, V., A. Shakal, C. Scrivner, E. Hauksson, J. Polet, and L. Jones (2002). TriNet strong-motion data from the M 7.1 Hector Mine, California, earthquake of 16 October 1999, *Bull. Seismol. Soc. Am.* **92**, no. 4, 1525–1541.
- Graves, R. W., and B. T. Aagaard (2011). Testing long-period ground-motion simulations of scenario earthquakes using the M_w 7.2 El Mayor-Cucapah mainshock: Evaluation of finite-fault rupture characterization and 3D seismic velocity models, *Bull. Seismol. Soc. Am.* **102**, no. 2, 895–907.
- Gregor, N., N. A. Abrahamson, G. M. Atkinson, D. M. Boore, Y. Bozorgnia, K. W. Campbell, B. S.-J. Chiou, I. M. Idriss, R. Kamai, E. Seyhan, et al. (2014). Comparison of NGA-West 2 GMPEs, *Earthq. Spectra* **30**, no. 3, 1179–1197.
- Hanks, T. C. (1975). Strong ground motion of the San Fernando, California, earthquake; ground displacements, *Bull. Seismol. Soc. Am.* **65**, no. 1, 193–225.
- Hatayama, K., and E. Kalkan (2012). Spatial amplification of long-period (3 to 16 s) ground-motions in and around the Los Angeles Basin during the 2010 M 7.2 El Mayor-Cucapah earthquake, *Proc. of the 15th World Conf. on Earthquake Engineering*, Lisbon, Portugal, 24–28 September 2012.
- Hruby, C. E., and I. A. Beresnev (2003). Empirical corrections for basin effect in stochastic ground-motion prediction, based on the Los Angeles basin analysis, *Bull. Seismol. Soc. Am.* **93**, no. 4, 1679–1690.
- Joyner, W. B. (2000). Strong motion from surface waves in deep sedimentary basins, *Bull. Seismol. Soc. Am.* **90**, S95–S112.
- Joyner, W. B., and D. M. Boore (1993). Methods for regression analysis of strong-motion data, *Bull. Seismol. Soc. Am.* **83**, no. 2, 469–487.
- Lee, V. W., M. D. Trifunac, M. I. Todorovska, and E. I. Novikova (1995). Empirical equations describing attenuation of peak of strong ground-motion, in terms of magnitude, distance, path effects and site conditions, *Department of Civil Engineering, University of Southern California, Rept. No. CE 95-02*, 269 pp.
- Li, Y. G., and J. E. Vidale (1996). Low-velocity fault-zone guided waves: Numerical investigations of trapping efficiency, *Bull. Seismol. Soc. Am.* **86**, 371–378.
- Mitchell, B. J., and H. J. Hwang (1987). Effect of low Q sediments and Crustal Q on L_g attenuation in the United States, *Bull. Seismol. Soc. Am.* **77**, no. 4, 1197–1210.
- Olsen, K. B. (2000). Site amplification in the Los Angeles basin from three-dimensional modeling of ground-motion, *Bull. Seismol. Soc. Am.* **90**, no. 6B, S77–S94.
- Sadigh, K., C. Y. Chang, J. A. Egan, F. Makdisi, and R. R. Youngs (1997). Attenuation relationships for shallow crustal earthquakes based on California strong motion data, *Seismol. Res. Lett.* **68**, no. 1, 180–189.
- Semblat, J. F., P. Dangla, M. Kham, and A. M. Duval (2002). Seismic effect for shallow and deep alluvial basins; in-depth motion and focusing effect, *Soil Dynam. Earthq. Eng.* **22**, nos. 9/12, 849–854.
- Singh, S., and R. B. Herrmann (1983). Regionalization of crustal coda Q in the continental United States, *J. Geophys. Res.* **88**, no. B1, 527–538.
- Spudich, P., W. B. Joyner, A. G. Lindh, D. M. Boore, B. M. Margaris, and J. B. Fletcher (1999). SEA99: A revised ground motion prediction relation for use in extensional tectonic regimes, *Bull. Seismol. Soc. Am.* **89**, no. 5, 1156–1170.
- Trifunac, M. D. (1994). Q and high-frequency strong motion spectra, *Soil Dynam. Earthq. Eng.* **13**, 149–161.
- Wills, C. J., M. Petersen, W. A. Bryant, M. Reichle, G. J. Saucedo, S. Tan, G. Taylor, and J. Treiman (2000). A site conditions map for California based on geology and shear-wave velocity, *Bull. Seismol. Soc. Am.* **90**, no. 6B, 187–208.
- Zhang, F., and A. S. Papageorgiou (2010). Attenuation characteristics of Taiwan: Estimation of coda Q , S -wave Q , scattering Q , intrinsic Q , and scattering coefficient, *Seismol. Res. Lett.* **81**, 769–777.

U.S. Nuclear Regulatory Commission
Mail Stop T-7F3
Washington, D.C. 20555-0001
vladimir.graizer@nrc.gov
(V.G.)

Earthquake Science Center
U.S. Geological Survey
Mail Stop 977
345 Middlefield Rd.
Menlo Park, California 94025
ekalkan@usgs.gov
(E.K.)

Manuscript received 29 January 2016;
Published Online 5 April 2016